

FIELD INVESTIGATIONS OF THE SHORT WAVE
MODULATION BY LONG WAVES

by

Shih-Tsan Tang

A DISSERTATION PRESENTED TO THE GRADUATE COUNCIL OF
THE UNIVERSITY OF FLORIDA
IN PARTIAL FULFILLMENT OF THE REQUIREMENTS FOR THE
DEGREE OF DOCTOR OF PHILOSOPHY

UNIVERSITY OF FLORIDA

1981

Bound by DOBBS BROS. LIBRARY BINDING CO., INC., St. Augustine, Florida

This dissertation is dedicated to Chi-Mei.

ACKNOWLEDGEMENTS

I would like to express my gratitude to Professor Omar H. Shemdin for his patient guidance, sincere encouragement and kind support throughout the course of this study.

Thanks are due to those who participated in the field measurement. I also wish to thank Drs. M. L. Banner, W. T. Liu and S. V. Hsiao for their helpful discussions and encouragement during my residence at Jet Propulsion Laboratory, California Institute of Technology.

I extend my thanks to Rena Herb and Cynthia Vey for their excellent effort in typing the manuscript, and to Lillean Pieter for her help in the drafting of the figures.

The work was sponsored by the Office of Naval Research under contract number N00014-81-F0069 and National Aeronautics and Space Administration under contract NAS7-100.

TABLE OF CONTENTS

	<u>Page</u>
ACKNOWLEDGEMENTS	iii
LIST OF FIGURES	vi
LIST OF TABLES	ix
ABSTRACT	x
<u>CHAPTER</u>	
I INTRODUCTION	1
1.1 Prologue	1
1.2 Scope of the Present Study	3
II THEORETICAL BACKGROUND	5
2.1 Momentum Transfer	5
2.2 Properties of High Frequency Waves	7
2.3 Two-Scale Model	11
2.4 Relaxation Model	13
III FIELD EXPERIMENT	20
3.1 Field Set-Up	20
3.2 Surface Wave Slope Measurement	26
3.3 Sea Surface Displacement Measurement	28
3.4 Current Measurements	28
3.5 Other Measurements	28
3.6 Data Acquisition and Digitization	29
IV DATA ANALYSIS	32
4.1 Spectral Analysis	32
4.2 Directional Spectrum Estimate	34
4.3 Determination of Surface Wave Slope	39
4.4 Demodulation Analysis	41
V EXPERIMENTAL RESULTS	49
5.1 Characteristics of Wave Slope Spectra	49
5.2 Modulation of Mean Square Slopes by Long Waves	59
5.3 Probability Density Function of Wave Slopes	61
5.4 Modulation of Short Waves by Long Waves	68

<u>CHAPTER</u>	<u>Page</u>
VI	DISCUSSION OF RESULTS 78
	6.1 Wave Slope Spectra 78
	6.2 Modulation of Mean Square Slopes 79
	6.3 Probability Density Function 80
	6.4 Hydrodynamic Modulation Level 80
VII	CONCLUSIONS AND RECOMMENDATIONS 86
	7.1 Conclusions 86
	7.2 Recommendations 87
 <u>APPENDICES</u>	
A	Algorithm for Estimating the Directional Wave Height Spectrum 89
B	Demodulation Procedure 96
REFERENCES 99
BIOGRAPHICAL SKETCH 103

LIST OF FIGURES

<u>Figure</u>	<u>Page</u>	
1	Schematic energy balance for the case of negligible dissipation in the main part of the spectrum. Q_{in} = atmospheric input, Q_{nl} = non-linear wave-wave transfer, Q_d = dissipation, and Q = net transfer (after Hasselmann <u>et al.</u> , 1973).	8
2	Hydrodynamic modulation transfer function for short gravity waves from relaxation model	18
3	Geographic location of the Noordwijk Tower. The contour lines are specified in fathoms	21
4	The wave follower in the wave following mode	22
5	Close view of the optical sensor mounted on the wave follower	23
6	Schematic diagram of the wave follower	24
7	Plan view of the relative location of sensors used in the wave follower experiment	25
8	The definition diagram of the refracted laser beam. The unit normal vector $\hat{n} = (\sin\gamma \cos\phi, \sin\gamma \sin\phi, \cos\gamma)$ defines the slope vector in x_1 and x_2 directions as $-\tan\gamma (\cos\phi, \sin\phi)$	27
9	Definition sketch of true direction. The true direction θ_a is the angle of V_a referred to the east counterclockwise . ^a	31
10	Sample time series measured by the electromagnetic current meter for Run 108	35
11	Sample time series for sea surface displacement and slope for Run 108	36
12	Frequency spectra for η and u for Run 108. The solid line gives the surface displacement spectrum. The dashed line gives the u -component of the orbital velocity spectrum . .	37
13	Attenuation of the orbital velocity. u/u_0 is the ratio of u -component of orbital velocity at 4.75 m below the mean sea level to that at the sea surface	38

<u>Figure</u>	<u>Page</u>
14	Calibration results for the deflection angle; $\bar{\gamma}$ is the calculated value 42
15	Calibration results for the azimuth angle; $\bar{\phi}$ is the calculated value 43
16	The down-wind slope spectrum for Run 108; EDF = 100 . . . 44
17	Probability density function (PDF) of the sea surface slope summarized from 40,000 points of Run 108. The open circles and solid points denote the PDF for down-wind slope and the cross-wind slope, respectively. The normalized slope is the ratio of the slope to the standard deviation. The solid curve is a Gaussian distribution with the same variance. The variance of down-wind slope is 0.0342 and that of cross-wind slope is 0.0310 45
18	An example of the sea surface displacement spectrum for "mixed sea" case. Run ID = 102, $U_a = 6.3$ m/s 50
19	Sea surface displacement spectrum of Run 328, a "well-defined peak" case. $U_a = 3.5$ m/s 51
20	Sea surface displacement spectrum of Run 325, a "well-defined peak" case. $U_a = 7.7$ m/s 52
21	The down-wind wave slope spectra 54
22	The frequency-weighted down-wind wave slope spectra . . . 56
23	The normalized down-wind wave slope spectra 57
24	Best fitted $\tilde{F}(U_{*})$ from the cases of "well-defined peak". . 58
25	Mean square wave slope as a function of the wind speed . . 60
26	The cross-correlation function of mean square down-wind wave slope and sea surface displacement for Run 325. The lag of the first peak in the cross-correlation defines τ_{\max} 62
27	The phase lead θ_{\max} as a function of wind speed U_a 63
28	Peak value of the normalized cross-correlation function as a function of wind speed. The open circles and solid points denote $\tilde{\rho}_{\max}$ values of "well-defined peak" cases and "mixed-sea" cases, respectively 64
29	Probability density function for Run 328. The notation used is the same as that in figure 17; $U_a = 3.5$ m/s; the variances are 0.0094 for down-wind wave slopes and 0.0101 for up-wind wave slopes 65

<u>Figure</u>		<u>Page</u>
30	Probability density function for Run 325. The notation used is the same as that in figure 17; $U_a = 7.7$ m/s; the variances are 0.0159 for down-wind wave slopes and 0.0314 for cross-wind wave slopes	66
31	Probability density function for Run 102. The notation used is the same as that in figure 17; $U_a = 6.3$ m/s; the variances are 0.0098 for down-wind slope and 0.0117 for cross-wind slopes	67
32	Hydrodynamic modulation level for Run 328. $U_a = 3.5$ m/s .	71
33	Hydrodynamic modulation level for Run 325. $U_a = 7.7$ m/s .	72
34	Hydrodynamic modulation level for Run 108. $U_a = 11.3$ m/s .	73
35	Hydrodynamic modulation level for 23 cm waves	74
36	Hydrodynamic modulation level for 8 cm waves	75
37	Hydrodynamic modulation level for 3 cm waves	76
38	Hydrodynamic modulation level for a "mixed-sea" case. Run ID = 102, $U_a = 6.3$ m/s	77
39	Comparison of hydrodynamic modulation level and modulus of radar modulation transfer function for $U_a = 3.5$ m/s . . .	82
40	Comparison of hydrodynamic modulation level and modulus of radar modulation transfer function for $U_a = 7.7$ m/s . . .	83
41	Comparison of hydrodynamic modulation level and modulus of radar modulation transfer function for $U_a = 11.3$ m/s . .	84

LIST OF TABLES

<u>Table</u>		<u>Page</u>
1	Summary of the Cases Selected for Detailed Data Analysis. .	30
2	Observed Values of the Significant Wave Height, Dominant Wind Direction and Tidal Current	46
3	Mean Square Wave Slopes and Sea Conditions	53
4	The Wavelength Bands for Modulation Study	69

Abstract of Dissertation Presented to the Graduate Council
of the University of Florida in Partial Fulfillment
of the Requirements for the Degree
of Doctor of Philosophy

FIELD INVESTIGATIONS OF THE SHORT WAVE MODULATION
BY LONG WAVES

Shih-Tsan Tang

December 1981

Chairman: Omar H. Shemdin
Major Department: Engineering Sciences

The study of short wave modulation by long waves has been carried out in the field. A laser-optical sensor is used to detect short wave slopes; a water surface displacement sensor and an electromagnetic current-meter are used to obtain sea surface wave directional spectra. Measured down-wind slope spectra are shown to be wind speed-dependent; the mean square wave slopes are generally larger than those measured by the sun glitter method.

A technique has been developed to account for the orbital motion due to two-dimensional waves. Hydrodynamic modulation levels are calculated for the wavelengths 3, 8 and 23 cm. A decrease in the modulation level is found with increasing wind speed. The results indicate that the hydrodynamic modulation is sufficiently strong at low wind speed to constitute a major radar imaging mechanism for ocean waves.

CHAPTER I INTRODUCTION

1.1 Prologue

The studies of the high frequency structure of surface waves have been receiving increased attention in recent years. This interest comes on the one hand from oceanographers who are interested in investigations of the momentum transfer at the air-sea interface and on the other hand from remote sensing scientists involved in interpretation of radar backscatter information from the sea surface.

When air blows over the water surface, momentum and energy are transferred to waves and currents. Wind-generated waves are described in a well-known survey by Ursell (1956) which concludes: "wind blowing over a water surface generates waves in the water by physical processes which cannot be regarded as known." Since then, many investigations followed to understand this complex phenomenon. Much progress towards understanding wave generation has been achieved since 1956, although our understanding of momentum transfer to current and to high frequency waves remains deficient.

It is well known that the momentum transfer plays a central role in the wave generation process by wind. From visual observation of surface waves we may consider the wind-generated wave system to consist of a spectrum of waves with a dominant wave frequency which shifts slowly with increasing wind speed and/or fetch, and a small-scale high frequency structure which is acted upon by wind and the orbital

velocities of long waves. Dissipation forces and the interactions among the dominant wave components also play important roles in the development of the whole wave system. If the small wave amplitudes are modulated by long waves, so is the wind stress (Keller and Wright, 1975); a modulated stress will contribute to the growth of the long waves. Hence, a detailed investigation of the short wave structure in the presence of long waves is essential to our understanding of the interacting processes at the air-sea interface.

From microwave backscatter point of view, the high frequency waves, which are of the order of centimeters in wavelength, scatter and reflect electromagnetic and acoustic waves impinging on the sea surface. These centimetric waves, characterized by their wavelengths, are associated with radar backscatter and formation of radar images of the ocean surface. The measurement of the imprint of ocean processes on the sea surface is attributed to the dynamics of waves with wavelengths of the same order as that of the radar. Because radar has limitations in observing long ocean waves (McLeish et al., 1980; Pawka et al., 1980), it is essential that further investigation of short wave dynamics be pursued.

By using sinusoidal long waves, it has been found, under laboratory conditions, that short waves undergo cyclic modulation in their wave height levels (Keller and Wright, 1975; Reece, 1978). In the field where the long waves are not monochromatic, the modulation of short waves has also been shown (Evans and Shemdin, 1980; Wright et al., 1980).

The radar observations by Wright et al. (1980) indicated that the modulation levels under field conditions cannot be explained by

straining of short waves by long waves alone and that additional forcing functions in addition to the straining must be considered. There is considerable evidence suggesting that radar backscatter can provide a direct measure of the hydrodynamic modulation and other characteristics of the short waves. There remains a need, however, for conclusive verification of such measurements. This study is motivated partially by the need to interpret radar backscatter from the sea surface and further in understanding the mechanisms responsible for imaging of ocean surface signatures with real and synthetic aperture radars.

1.2 Scope of the Present Study

The work reported in this dissertation is in response to the need to measure wave slopes in the field to obtain insight on the general characteristics of high frequency waves. Particular care is taken to obtain the hydrodynamic modulation levels.

Because the height of short waves is only a fraction of that of the long waves, a conventional wave gauge does not have sufficient resolution and satisfactory frequency response to provide a quantitative measurement of short waves. However, the sea surface wave slope, where the wave amplitude is tuned by the wavenumber, provides a measure that is of the same order of magnitude for both long and short waves. In the analysis phase of this investigation, the long wave directional properties are considered and the hydrodynamic modulation levels of short waves are estimated for each long wave frequency component.

A theoretical survey is given in chapter 2. The experimental set-up and field conditions are described in chapter 3. Chapter 4 shows the general scheme for data analysis and provides sample results. The experimental results are shown in chapter 5. A discussion of results is given in chapter 6. Finally, conclusions and recommendations are given in chapter 7.

CHAPTER II THEORETICAL BACKGROUND

2.1 Momentum Transfer

The generation of waves by wind is a significant geophysical phenomenon that has received considerable interest in recent years. The wind-wave generation mechanisms proposed by Phillips (1957) and Miles (1957) constitute significant contributions towards understanding the processes by which wind generates waves. The initial phase of wave generation is associated with the turbulent aspects of wind over the air-sea interface. Phillips (1957) postulates that waves are generated by the normal stress fluctuations associated with a turbulent wind. He suggests that the pressure field "resonates" with the wave field as long as both the speed and length of the pressure field match those of surface waves. His resonance mechanism predicts a linear energy growth rate which is consistent with field observations in the initial phase of the wind generation process. The mechanism proposed by Miles (1957) suggests that the energy transfer from wind to waves is primarily due to the wind-induced pressure perturbation in the atmospheric shear flow. Miles' shear flow instability mechanism yields an exponential growth rate of surface wave energy. Later, Miles (1960) combined the two mechanisms discussed above to account for both the initial and subsequent growth rates of surface waves.

The field investigations of Snyder and Cox (1966) and Barnett and Wilkerson (1967) concluded that Phillips' theory could account for wave growth only if the atmospheric pressure fluctuation was increased by a factor of 50. They also found the principal stage of wave spectral development to occur at the rate with an order of magnitude greater than that predicted by Miles' (1960) theory. These discrepancies motivated new investigations to re-examine the mechanism involved in atmospheric transfer from wind to waves.

Townsend (1972) re-evaluated the momentum transfer by solving the linearized equation for turbulent flow over a progressive wave numerically. He found the momentum transfer from wind to waves to be of the same order as that predicted by Miles' theory. Gent and Taylor (1976) extended Townsend's work by including the nonlinear terms in the governing equation. They showed the air flow pattern and shear stress vary along the wave profile. The shear stress was found to have a strong peak at the crest; they also suggested that the momentum transfer rate is significantly enhanced if the surface roughness is to vary along the long wave profile. An enhanced momentum transfer rate associated with the flow separation over breaking waves was suggested by Banner and Melville (1976). The possibility of patches of concentrated momentum transfer from air to water was first introduced by Dorman and Mollo-Christensen (1973) following acquisition of an extensive set of field measurements.

A nonlinear wave-wave interaction mechanism has been invoked that indicates transfer of energy from the high frequency part of a wave spectrum to the peak and forward face of the spectrum. This mechanism offers a satisfactory explanation of the rapid growth rate

of waves observed in the field. Figure 1 shows the schematic representation of the energy balance proposed by Hasselmann et al. (1973). The nonlinear wave-wave interaction process redistributes energy from frequencies higher than the peak frequency to those lower than the peak of the spectrum. The nonlinear energy input (Q_{in}) to the high frequency part is cancelled by the dissipative process (Q_d), and the main role of the wave-wave interactions (Q_{nl}) appears to be energy transfer toward the low frequency forward face of the energy spectrum. The nonlinear wave-wave interaction can explain the rapid growth rates observed by Snyder and Cox (1966) and Barnett and Wilkerson (1967). A simplified mechanism for energy transfer from short waves to long waves was explored by Longuet-Higgins and Stewart (1960, 1964). This will be discussed in section 2.3.

2.2 Properties of High Frequency Waves

The energy of waves in the capillary and short gravity wave range is better characterized by the slope spectrum rather than by the surface displacement spectrum. The high frequency waves are small in amplitude and large in wavenumber; the wave slope, which is proportional to the product of these two wave parameters, is a significant quantity throughout the spectral range. Hence, the slope is more easily measured in the high frequency range of waves compared to wave amplitude.

The shape of the high frequency portion of the wave height spectrum was proposed by Phillips (1958) based on dimensional analysis and similarity considerations as follows

$$E(f) = (2\pi)^{-4} \beta g^2 f^{-5} , \quad (2.1)$$

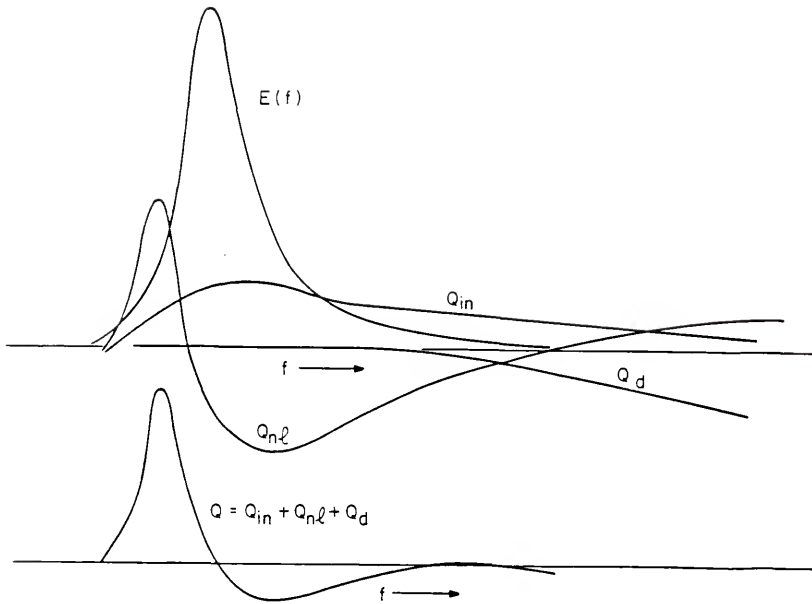


Fig. 1 Schematic energy balance for the case of negligible dissipation in the main part of the spectrum. Q_{in} = atmospheric input, Q_{nl} = non-linear wave-wave transfer, Q_d = dissipation, and $Q = Q_{in} + Q_{nl} + Q_d$ = net transfer (after Hasselmann *et al.*, 1973).

where β is the equilibrium constant, f is the circular frequency and g is the gravitational acceleration. The constancy of β has been questioned by many investigators (Liu, 1971; Hasselmann et al., 1973; Mitsuyasu, 1977). Various other spectral forms for the high frequency range of waves have been proposed; Pierson (1976), for example, summarized Mitsuyasu and Honda's (1974) laboratory results by proposing a displacement spectrum for the high-frequency range of the form

$$E(f) = 0.1393 f^{-b} \quad , \quad (2.2)$$

where

$$b = 5 - \log_{10}(U_*^2) \quad , \quad (2.3)$$

and U_* is the friction velocity of the wind. However, the spectral form shown in equation (2.2) does not follow Phillips' inverse fifth power law shown in equation (2.1).

In the capillary wave range, if the viscous dissipation is not important the equilibrium shape can be derived on dimensional grounds as

$$E(f) = A \left(\frac{\Gamma}{\rho}\right)^{2/3} f^{-7/3} \quad , \quad (2.4)$$

where A is a constant and Γ is surface tension.

The equilibrium range in the wave slope spectrum for both gravity and capillary waves was derived by Phillips (1977, p. 152) from dimensional considerations

$$S(f) = Df^{-1} \quad , \quad (2.5)$$

where D is a constant but may assume different values for gravity and capillary spectral ranges.

Cox (1958) used an optical-refraction technique to measure capillary wave slopes. He found the mean square slopes increase rapidly with wind speed. His results, however, do not show clearly the wave spectral dependence on wind speed. Wu (1971) provided useful information on the wave slope distribution function by using an optical reflection technique in a laboratory facility. He found the shapes of the distribution function to be Gaussian in general. Long and Huang (1976) measured the wave slopes using a laser device. They concluded that equation (2.5) is valid in the capillary-gravity range; the spectra showed similar shapes and no obvious dependence on wind speed. A recent experiment by Leonart and Blackman (1980) clearly shows the wind dependence in spectra of capillary waves. They proposed the wind dependence of the down-wind slope spectrum to have the form

$$S(f) = D_2 \left(\frac{\rho U_* v}{T} \right)^{1/2} f^{-1}, \quad (2.6)$$

where $D_2 = 2.95 \times 10^{-1}$ and v is kinematic viscosity of water.

The experiments discussed above were all conducted in the laboratory. It is noted that only few wave slope measurements are available under field conditions. Cox and Munk (1954) used a photographic and optical reflection technique to infer the character of wave slopes from sun glitter patterns. They showed that the mean square slope is wind-dependent. The cross-wind slope was found to be slightly more peaked than the Gaussian distribution;

the down-wind slope distribution peak was found to be shifted by 2.5 degrees in the down-wind direction.

2.3 Two-Scale Model

In a first examination of the interaction of short waves and long waves, Longuet-Higgins and Stewart (1960) considered the hydrodynamic interaction of two gravity waves noncontiguous in the frequency domain with no energy input nor dissipation. They pursued a perturbation analysis to find that, correct to the second order, the free surface in deep water can be described by

$$\eta = a_s \sin \chi_s (1 + a_l k_l \sin \chi_l) - a_s \cos \chi_s (a_l k_s \cos \chi_l) \quad , \quad (2.7)$$

where χ is the phase of the progressive wave, a is the wave amplitude, k is the wavenumber; the subscripts s and l denote the properties of short waves and long waves, respectively, and $k_s \gg k_l$ is assumed.

Equation (2.7) represents a modulated amplitude

$$a'_s = a_s (1 + a_l k_l \sin \chi_l) \quad , \quad (2.8)$$

and a modulated wavenumber

$$k'_s = k_s (1 + a_l k_l \sin \chi_l) \quad . \quad (2.9)$$

This means that both the amplitude and the wavenumber vary in phase with the long wave profile. The results shown in equations (2.8) and (2.9) represent the effect of the compression of the orbital velocity of the long wave and the work done by the long waves against the radiation stress of the short waves.

Phillips (1963) indicated that the energy dissipated by the short waves is acquired from the long waves so that the interaction of short waves with long waves would dampen the long waves. On the other hand, Longuet-Higgins (1969) pointed out that as the short waves dissipate their energy, they impart their momentum to the long waves and thus exert a stress which is in phase with the orbital velocity of the long waves; the latter should lead to the growth of the long waves. He also showed that if the short waves were continuously regenerated by the wind, the input of energy due to this "maser-type" mechanism should be more significant than other competing mechanisms.

Hasselmann (1971) showed that the energy gain of long waves predicted by Longuet-Higgins (1969) is cancelled by the potential energy transfer, hence resulting in a weak decay of the long waves. Garrett and Smith (1976) reported that the long wave growth can result from the interaction of short waves with long waves provided the short wave generation is correlated with the orbital velocity of the long waves.

All of the above analyses have been with two-scale motions where each scale is represented by a monochromatic wave. In a wind-wave situation we have a spectrum of short waves modulated by a spectrum of long waves. A simplified version, the modulation of a spectrum of short waves by a monochromatic long wave, can be simulated under laboratory conditions (Mitsuyasu, 1966; Reece, 1978). A refined model, originated from the radar measurements by Keller and Wright (1975), will be discussed more fully in the next section.

2.4 Relaxation Model

Keller and Wright (1975) first proposed a relaxation model to interpret their microwave measurement of the modulation of wind-generated short waves by longer plunger-generated waves. The basis of their relaxation model is that in an equilibrium situation, with a known distribution function, any departure of the system from the equilibrium induced by external forces, results in a return to equilibrium at an exponential rate. Their measurements are based on radar backscattering, in which the short waves represent the Bragg-scattering waves, through the relation

$$k_s = 2k_r \cos \theta_d \quad , \quad (2.10)$$

where k_s is the wavenumber of the short waves, k_r is the radar wavenumber, and θ_d is the depression angle. They specify the energy spectrum in the wavenumber domain and treat the hydrodynamic interaction between the short wave and long wave through the use of the radiative transport equation in which the energy spectrum of the short waves is modulated by a long monochromatic wave. The transport equation, which includes the effect of the horizontal orbital current component, for the short wave-long wave interaction can be written as

$$\frac{dF}{dt}(k_s, x, t) + \gamma_1 F \frac{\partial U_0}{\partial x} = Q \quad , \quad (2.11)$$

where F is the short wave energy spectrum in wavenumber space, γ_1 is the Longuet-Higgins' strain factor (Longuet-Higgins and Stewart, 1964) given by

$$\gamma_1(k_s) = \frac{1 + (3\Gamma k_s^2/\rho g)}{2(1 + (\Gamma k_s^2/\rho g))} , \quad (2.12)$$

U_0 is the horizontal component of the long wave orbital velocity given by

$$U_0(x, t) = U_{\ell} e^{i(k_{\ell} x - \omega_{\ell} t)} . \quad (2.13)$$

The source term Q on the right hand side of equation (2.11) represents the energy input from the wind, nonlinear dissipation and wave-wave interaction. The energy input from the wind is assumed to be βF , where β is the exponential growth rate. Equation (2.11) can be written as

$$\frac{\partial F}{\partial t} + \frac{\partial F}{\partial k_s} \dot{k}_s + \frac{\partial F}{\partial x} \dot{x} + \gamma_1 F \frac{\partial U_0}{\partial x} = \beta F + H , \quad (2.14)$$

where the dot operator represents derivative with respect to time.

The functional $H(F, k_s)$ accounts for the nonlinear energy dissipation and the energy transfer due to wave-wave interactions. The conservation of waves gives

$$\dot{k}_s = - \frac{\partial \omega_s}{\partial x} . \quad (2.15)$$

The dispersion relation is modified by the underlying current such that

$$\omega_s = \sigma_s(k_s) = k_s(U_0(x, t) + U_m) , \quad (2.16)$$

where σ_s is the intrinsic frequency, U_m is the medium speed contributed by the tidal current and the wind drift. Also, the group velocity

C_{gs} is given by

$$\dot{x} = C_{gs} . \quad (2.17)$$

Equation (2.11) becomes

$$\frac{\partial F}{\partial t} + C_{gs} \frac{\partial F}{\partial x} - k_s \frac{\partial U_0}{\partial x} \frac{\partial F}{\partial k_s} + \gamma_1 F \frac{\partial U_0}{\partial x} = \beta F + H . \quad (2.18)$$

In the frame moving with the long wave phase speed, C_λ , the following transformation can be made

$$\frac{\partial}{\partial x} \rightarrow \frac{\partial}{\partial x} , \quad (2.19)$$

$$\frac{\partial}{\partial t} \rightarrow \frac{\partial}{\partial t} - C_\lambda \frac{\partial}{\partial x} , \quad (2.20)$$

$$U_0(x, t) \rightarrow U_0(x) = U_\lambda e^{ik_\lambda x} . \quad (2.21)$$

For the stationary case in the moving frame, equation (2.18) becomes

$$-(C_\lambda - C_{gs}) \frac{\partial F}{\partial x} + (\gamma_1 F - k_s \frac{\partial F}{\partial k_s}) \frac{\partial U_0}{\partial x} = \beta F + H . \quad (2.22)$$

If F and H are expanded in terms of ϵ , where

$$\epsilon = U_\lambda / C_\lambda , \quad (2.23)$$

which is of the same order as the long wave slope,

$$F = F^{(0)}(k_s) + \epsilon F^{(1)}(k_s, x) + \dots \quad (2.24)$$

$$H = H^{(0)} + \epsilon H^{(1)} + \dots , \quad (2.25)$$

equation (2.22) gives the zeroth-order equation

$$\beta F^{(0)} = H^{(0)} , \quad (2.26)$$

which can be interpreted as the energy input from the wind is being balanced by dissipation due to nonlinear wave-wave transfer.

The terms proportional to ε give to first order equation

$$\begin{aligned} -\left(1 - \frac{C_{gs}}{C}\right) \frac{\partial F(1)}{\partial x} - ik_s k_\lambda \frac{\partial F(0)}{\partial k_s} e^{ik_\lambda x} + i\gamma_1 k_\lambda F(0) \\ = \frac{\beta}{C_\lambda} F(1) + \frac{H(1)}{C_\lambda} \end{aligned} \quad (2.27)$$

In the relaxation model, the relaxation rate μ is introduced such that

$$H(1) = (-\beta - \mu) F(1) \quad (2.28)$$

Letting

$$F(1) = f(1) e^{ik_\lambda x}, \quad (2.29)$$

$f(1)$ can be solved by substituting equation (2.28) into equation (2.27)

$$M \equiv \frac{f(1)}{F(0)} = \frac{\sigma_\lambda \left(\frac{k_s}{F(0)} \frac{\partial F(0)}{\partial k_s} - \gamma_1 \right)}{\mu^2 + (\sigma_\lambda - k_\lambda C_{gs})^2} \left[(k_\lambda C_{gs} - \sigma_\lambda) + i\mu \right], \quad (2.30)$$

where σ_λ is the radian frequency of the long wave. Combining equations (2.25), (2.29) and (2.30) it follows that

$$F = F(0) \left(1 + \frac{U}{C} Me^{iX_\lambda} \right), \quad (2.31)$$

correct to the first order, where X_λ is the long wave phase angle.

Since M is a complex number in general, its modulus $|M|$ is called the hydrodynamic modulation level, its argument θ_{mod} gives the phase information of $F(1)$ relative to the long wave crest.

In fact, the long wave phase speed is much greater than C_{gs} , i.e.

$$\sigma_\lambda / k_\lambda \gg C_{gs}, \quad (2.32)$$

and therefore, equation (2.30) can be written as

$$\begin{aligned}
 M &= \frac{\sigma_{\ell} \left(\frac{k_s}{F(0)} \frac{\partial F(0)}{\partial k_s} - \gamma_1 \right)}{\mu^2 + \sigma_{\ell}^2} (-\sigma_{\ell} + i\mu) \\
 &= \frac{\frac{k_s}{F(0)} \frac{\partial F(0)}{\partial k_s} - \gamma_1}{\left(1 + \left(\frac{\mu}{\sigma_{\ell}}\right)^2\right)} \left(-1 + i \frac{\mu}{\sigma_{\ell}}\right) \quad (2.33)
 \end{aligned}$$

Assuming a Phillips' spectrum of the form $F(k_s) \sim k_s^{-4}$ (Phillips, 1977, p. 145) the hydrodynamic modulation for the short gravity wave where $\gamma_1 = 0.5$ is

$$M = 4.5 \frac{\sigma_{\ell}}{\mu} \frac{(\sigma_{\ell}/\mu - i)}{1 + (\sigma_{\ell}/\mu)^2} \quad (2.34)$$

The variation in hydrodynamic modulation ranges from 0 at low σ_{ℓ}/μ and asymptotically approaches 4.5 at high σ_{ℓ}/μ . Figure 2 displays M given in equation (2.34). Alpers and Hasselmann (1978) used the ratio of the group velocity of the short wave to the group velocity of the long wave and the long wave slope as the expansion parameters in the action balance equation. Their solution is equivalent to equation (2.33) where it is further assumed the long wave phase speed is much greater than the short wave group speed.

In investigations of radar backscatter from the sea surface Keller and Wright (1975), Wright *et al.* (1980), and Plant (1980) proposed the modulation of microwave power backscattering from the Bragg-waves, $P(t)$, to have the form

$$P(t) = \bar{P} \left(1 + M_{\text{radar}} \left(\frac{U_{\ell}}{C_{\ell}} \right) e^{iX_{\ell}} \right), \quad (2.35)$$

where \bar{P} is the mean backscattered power. For the natural environment the radar modulation transfer function was generalized to the form

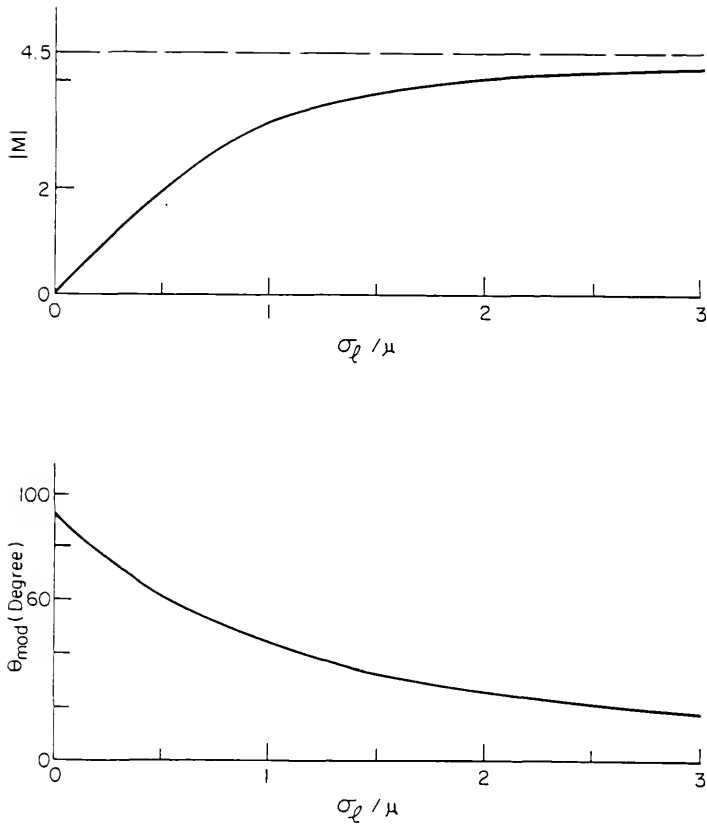


Fig. 2 Hydrodynamic modulation transfer function for short gravity waves from relaxation model.

$$M_{\text{radar}} = \frac{C_{\lambda}}{p} \frac{E_{p\tilde{v}}}{E_{\tilde{v}\tilde{v}}} , \quad (2.36)$$

where $E_{p\tilde{v}}$ is the cross-spectrum of the instantaneous received power and instantaneous line of sight speed \tilde{v} and $E_{\tilde{v}\tilde{v}}$ is the auto-spectrum of the line of sight speed. $\tilde{v}(t)$ can be detected directly from the instantaneous Doppler shift of the backscattered signal.

CHAPTER III FIELD EXPERIMENT

3.1 Field Set-Up

During September to November of 1979, the wave follower was operated from the Noordwijk research tower located approximately 10 km offshore of the coast of Holland in 18 m water depth as an element of the Maritime Remote Sensing Experiment (MARSEN). The field operations were described by Shemdin (1981). Figure 3 shows the geographic location of the Noordwijk tower. Figures 4 and 5 show the wave follower deployed from the Noordwijk tower in a data acquisition mode.

The wave follower is a servo-driven electric motor that powers an endless cable on which instruments are mounted. The general features of the wave follower were described by Shemdin (1981). The mechanism is shown schematically in figure 6. The instrument frame was designed to follow a wave profile 6 m in height and 3 sec in period. The capacitance wave height gauge attached to the wave follower frame provides the drive signal to the servo motor which then vertically translates the instrument frame to maintain the capacitance gauge at a constant submergence depth. In the field, the latter was accomplished to within an error of ± 5.0 cm.

The measurements obtained by mounting instruments on the wave follower are discussed in the following. A plan view showing relative positions of instruments is given in figure 7.

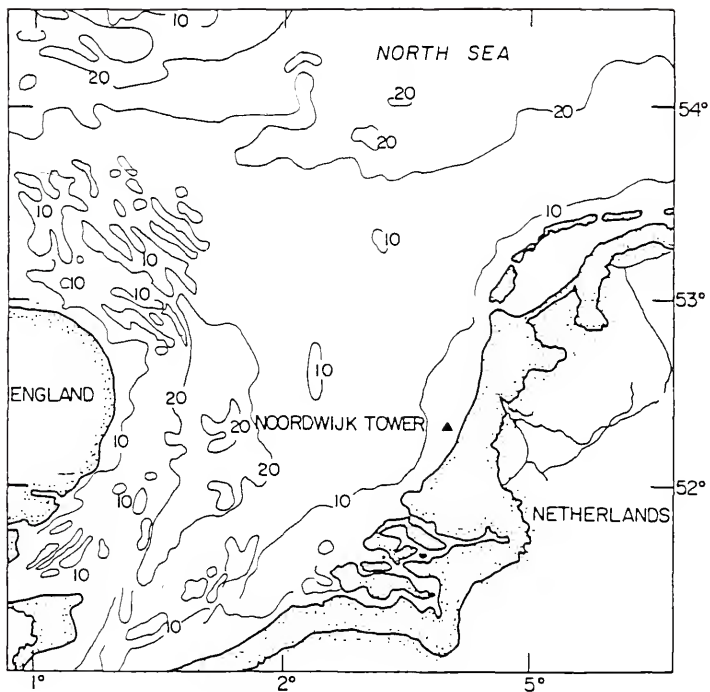


Fig. 3 Geographic location of the Noordwijk Tower. The contour lines are specified in fathoms.

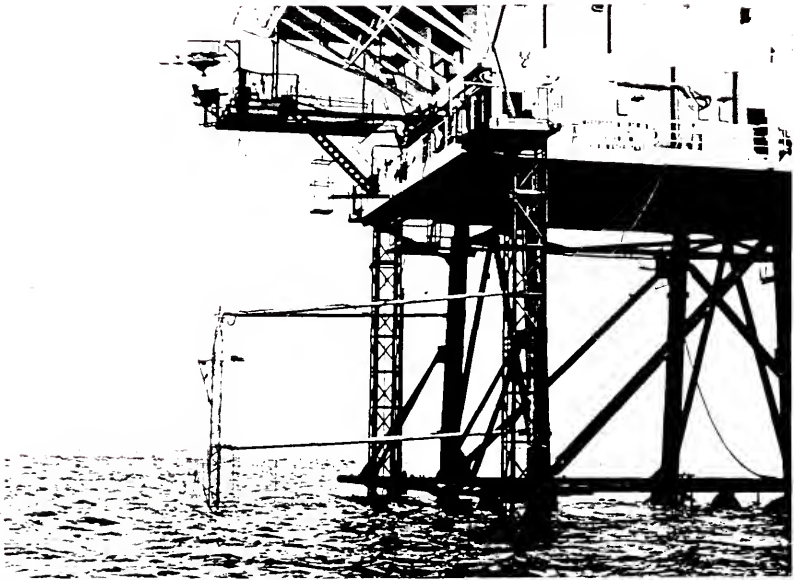


Fig. 4 The wave follower in the wave following mode.

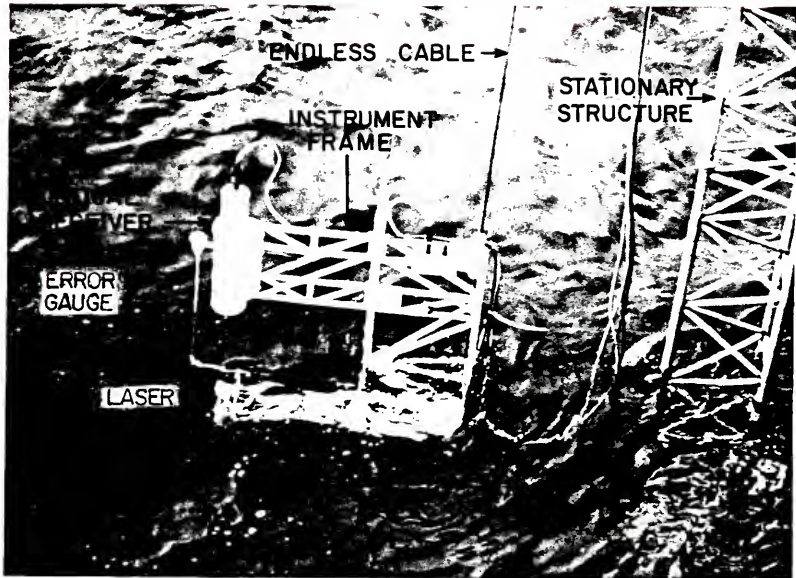


Fig. 5 Close view of the optical sensor mounted on the wave follower.

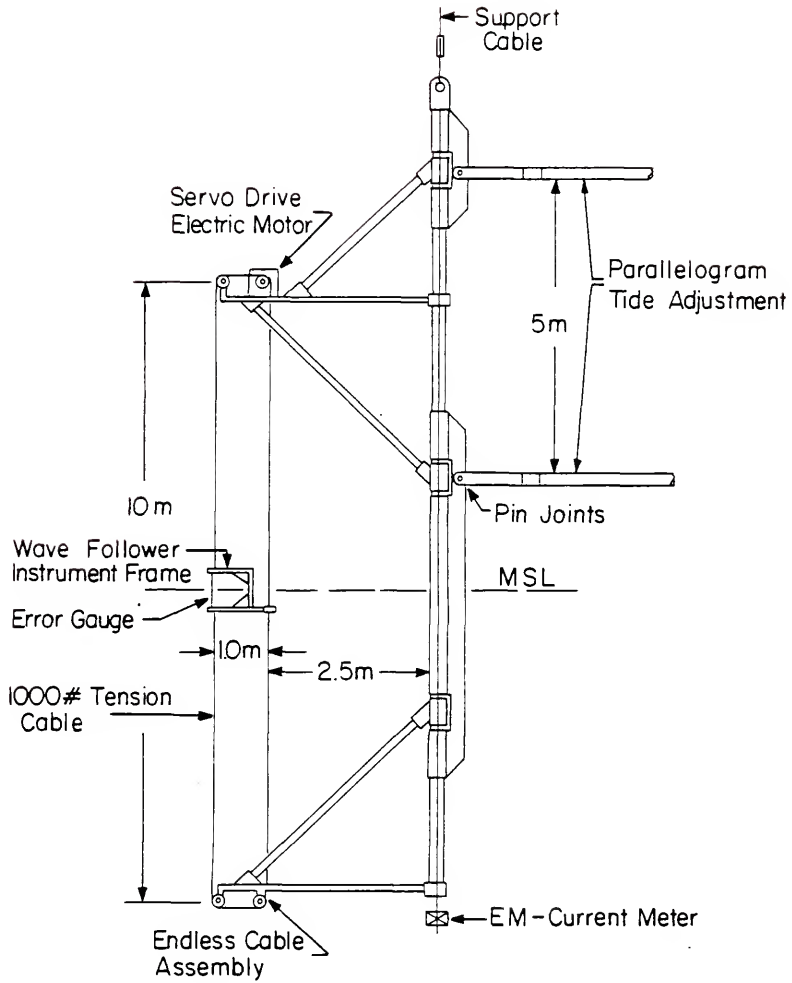


Fig. 6 Schematic diagram of the wave follower.

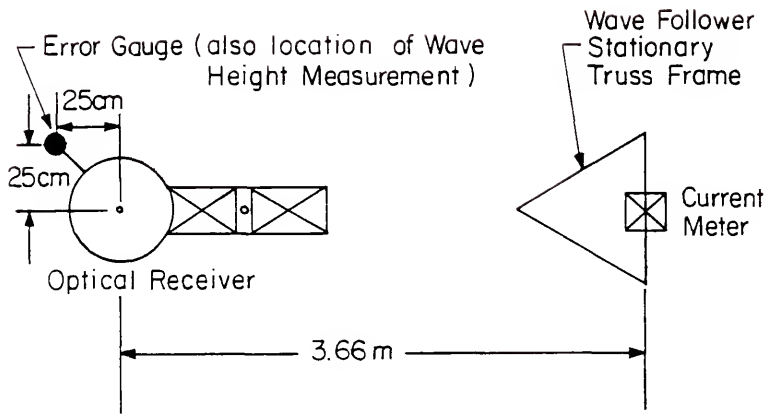


Fig. 7 Plan view of the relative location of sensors used in the wave follower experiment.

3.2 Surface Wave Slope Measurement

A high-response laser-optical sensor developed at the University of Florida (Tober, Anderson and Shemdin, 1973; Palm, 1975) was used to obtain time series of the sea surface slope at a point location. A vertically oriented laser beam emanates from a laser mounted on the wave follower instrument frame below the water surface. The refracted laser beam in air is then related to the water surface normal which is defined by an azimuth angle (ϕ) and a deflection angle (γ), as shown in figure 8. If the unit surface normal vector is denoted by \hat{n} , its components are specified by

$$\hat{n} = (\sin\gamma \cos\phi, \sin\gamma \sin\phi, \cos\gamma) . \quad (3.1)$$

The sea surface at a fixed time can be specified by

$$\psi(x_1, x_2, x_3) = x_3 - \eta(x_1, x_2) = 0 , \quad (3.2)$$

where x_i ($i=1, 2, 3$) are the three spatial coordinates and η is the sea surface displacement. The unit normal vector to the surface ψ is given by

$$\hat{n} = \nabla\psi / |\nabla\psi| = (-\partial\eta/\partial x_1, -\partial\eta/\partial x_2, 1) / |\nabla\psi| . \quad (3.3)$$

Equations (3.1) and (3.3) give the slope components along two major axes,

$$(\partial\eta/\partial x_1, \partial\eta/\partial x_2) = -\tan\gamma (\cos\phi, \sin\phi) . \quad (3.4)$$

The down-wind slope is given by the scalar product of the unit vector pointing in the down-wind direction and the slope vector given in equation (3.4). For example, if α denotes the wind direction

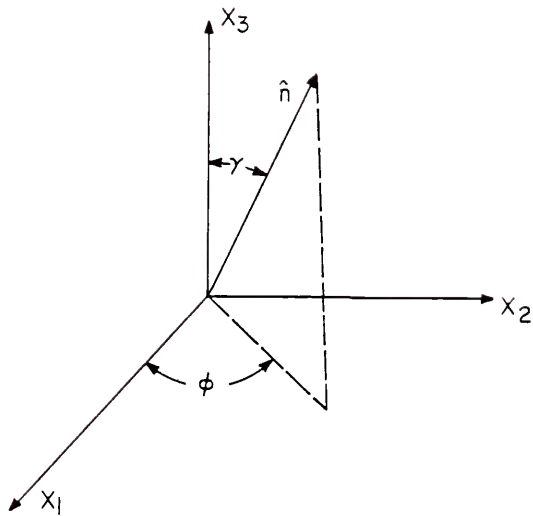


Fig. 8 The definition diagram of the refracted laser beam. The unit normal vector $\hat{n} = (\sin\gamma \cos\phi, \sin\gamma \sin\phi, \cos\gamma)$ defines the slope vector in x_1 and x_2 directions as $-\tan\gamma (\cos\phi, \sin\phi)$.

referred to the x_1 axis then the down-wind slope is given by

$$s = -\tan\gamma \cos(\phi-\alpha) . \quad (3.5)$$

3.3 Sea Surface Displacement Measurement

A linear displacement sensor which measures the vertical position of the wave follower instrument frame was used to detect the sea surface displacement. Let the displacement signal be V_1 and the error signal be V_2 , the sea surface displacement is given simply by

$$n(t) = \alpha_1 V_1(t) + \alpha_2 V_2(t) , \quad (3.6)$$

where t is time, α_1 and α_2 are calibration constants.

3.4 Current Measurements

Two horizontal components of current were measured at an Eulerian level of 4.75 m below the mean sea level and at a position located 3.66 m from the wave slope sensor (see figure 7). The electromagnetic current meter was mounted on the lower extremity of the stationary structural frame of the wave follower, shown in figure 6. Hence, the current was measured only in an Eulerian mode. It is noted that the electromagnetic current meter measured the tidal component of the current as well as the wave orbital velocity (Olson, 1972).

3.5 Other Measurements

In addition to the above, wind speed and direction were obtained from an anemometer located at 10 m above the mean sea level.

3.6 Data Acquisition and Digitization

Eight channels of data were recorded on the AMPEX PR-2000 Instrumentation Recorder. These included four slope signals which give the position of the refracted laser beam, two current signals, one displacement signal and one error signal. The author has been responsible for the work of the analog-to-digital conversion and thereafter.

The analog signal tapes were digitized at 400 sps (samples per second) to account for the high frequency encounter of small scale waves. The sampling rates for the current and sea surface displacement measurements were reduced to increase computational efficiency. The method used was to take the arithmetic mean of the values of neighboring data points.

After careful examination of the strip chart records generated during the data digitization process, twelve cases were selected for detailed analysis. They are summarized in Table 1. In this table wind direction is given with respect to a reference frame specified in figure 9. Hence, in Run 325 wind direction of 295 degrees refers to wind towards 295 degrees (southeast) from east in a counter-clockwise sense or from direction 115 degrees (northwest) in the same sense.

Table 1
 Summary of the Cases Selected for Detailed Data Analysis

Date	Time (1)	Run ID	Wind		Number of data point (3)
			speed (m/s)	direction (deg) (2)	
9/27	15:50	325	7.7	295	648,335
9/27	16:36	326	7.5	291	426,466
9/28	9:55	327	3.0	163	261,239
9/28	14:41	328	3.5	249	482,092
10/2	13:34	102	6.3	150	719,328
10/11	5:26	106	5.9	39	632,079
10/11	7:29	110	4.3	54	339,725
10/18	22:05	107	5.4	329	494,665
10/19	10:33	108	11.3	50	548,259
10/19	14:13 (4)	105	12.7	48	158,369
11/19	20:02	217	4.5	300	513,334
11/19	20:53	104	5.0	273	724,662

Note: (1) Local time. (2) True direction, direction referred to the east counterclockwise (see figure 9). (3) Sampling rate = 400 sps. (4) 011 slick experiment.

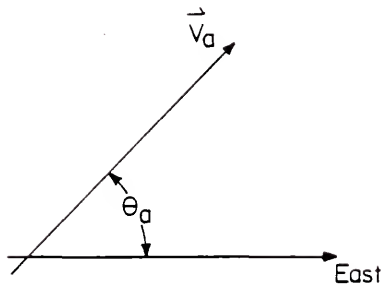


Fig. 9 Definition Sketch of true direction. The true direction θ_a is the angle of \vec{V}_a referred to the east counterclockwise.^a

CHAPTER IV DATA ANALYSIS

The digitized data gave digital representation of voltages for each of the sensors used. Before useful quantities could be obtained the voltages had to be converted to the physical quantities they were measuring by applying their calibration relationships. Following these steps, various calculations were conducted to achieve specific goals of this study. In the following the various algorithms used in the study are discussed.

4.1 Spectral Analysis

For a time series $y(t)$ of duration T , sampled at N times, with time interval Δ so that $T=N\Delta$, the corresponding discrete Fourier transform is (Newland, 1975)

$$Y_n = \frac{1}{N} \sum_{j=0}^{N-1} y_j \exp(-i 2\pi j n/N) , \quad (4.1)$$

where

$$y_j = y(j\Delta), \quad i^2 = -1 \text{ and } n = 0, 1, \dots, N-1.$$

Its inverse transform is

$$y_j = \sum_{n=0}^{N-1} Y_n \exp(i 2\pi j n/N) \quad (4.2)$$

with $j = 0, 1, \dots, N-1$.

In this study, a FFT routine (Krogh, 1970) was called to calculate Y_n for a given discrete time series y_j . This routine was capable of calculating the inverse Fourier transform shown in equation (4.2).

An algorithm suggested by Welch (1967) was used to estimate the properties of the energy spectrum for this study. In brief, a time series was divided into K segments, each with length L , and the discrete Fourier transform for each k th segment was performed according to

$$Y_n^K = \frac{1}{L} \sum_{j=0}^{L-1} y_j^K W_j \exp(-i 2\pi j n/L), \quad (4.3)$$

where W is the window function given by

$$W_j = 1 - \left[1 - \frac{2(j+1)}{L+1} \right]^2. \quad (4.4)$$

The estimate of the spectrum for the k th segment was given by

$$I_n^K = \frac{L |Y_n^K|^2}{\sum_{j=0}^{L-1} W_j^2}. \quad (4.5)$$

The final estimate of energy spectrum was obtained by averaging the I_n^K 's given in equation (4.5).

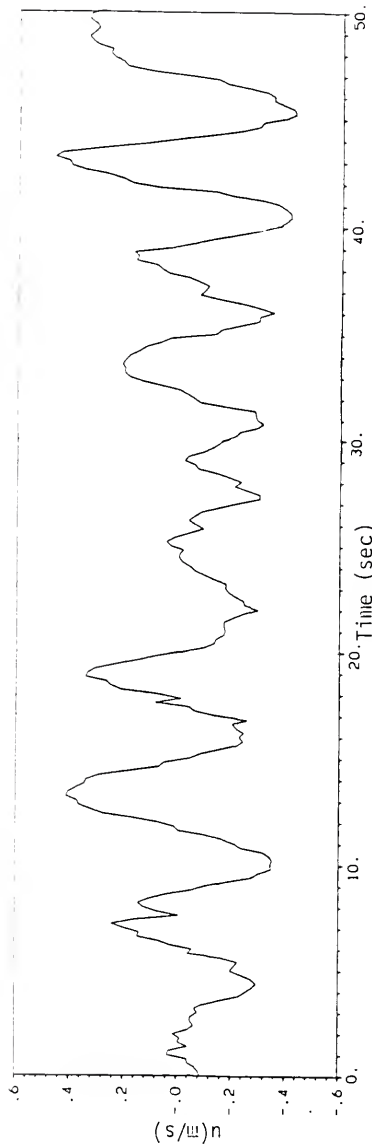
The discrete Fourier transform technique was extensively used in this study such as in the cross-spectrum analysis, the demodulation of the wave slope signals, and the calculation of the orbital velocity. The energy spectral estimates by the segment averaging method was used to determine the slope spectrum, the orbital velocity spectrum and the wave height spectrum.

Various K and L values were used for the different calculations. They will be stated in the text under related discussions. The equivalent degrees of freedom (EDF) using this procedure is $2 \times K$ (Welch, 1967).

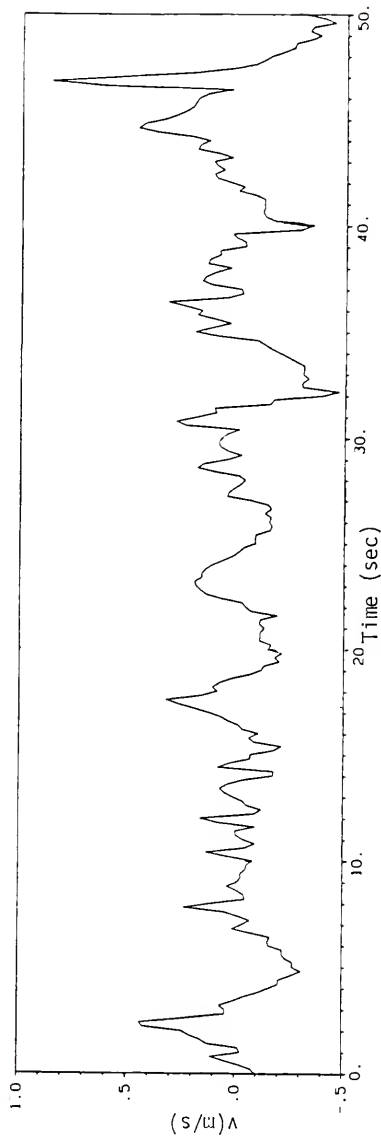
4.2 Directional Spectral Estimates

Waves, as they occur in nature, are random and two-dimensional, in appearance and, as such, have to be treated as a statistical phenomenon. The current meter used during the experiment served a dual purpose: (1) to detect the component of orbital current due to the long surface waves, and (2) to measure the tidal component of current. The capability to measure both the long waves orbital velocity and the low frequency ($f < 10^{-2}$ Hz) tidal fluctuations was reported by Olson (1972) and Winant and Olson (1976).

In this study, we use a high-pass filter to obtain the component of current due to waves; the cut-off frequency was set at 0.02 Hz. Figures 10 and 11 show typical time series of the sea surface displacement, η , and the current components u and v . The corresponding spectra for η and u are shown in figure 12 ($K=10$ and $EDF=20$). The close agreement between the spectra $E_{\eta\eta}$ and E_{uu} suggests that electromagnetic current meter provides reasonable measurement of the orbital velocity of surface waves. It is noted that the current meter was located at 4.75 m below the mean sea level. The orbital velocity due to waves at this level are attenuated to less than 20% of the surface value for waves with frequencies greater than 0.3 Hz. Figure 13 gives exact attenuation values of various wave frequencies. Hence it was anticipated that the current meter would not detect orbital velocity components with frequencies greater than 0.3 Hz.



a. The u-component of the orbital velocity after removal of the mean tidal current.



b. The v-component of the orbital velocity after removal of the mean tidal current.

Fig. 10 Sample time series measured by the electromagnetic current meter for Run 103.

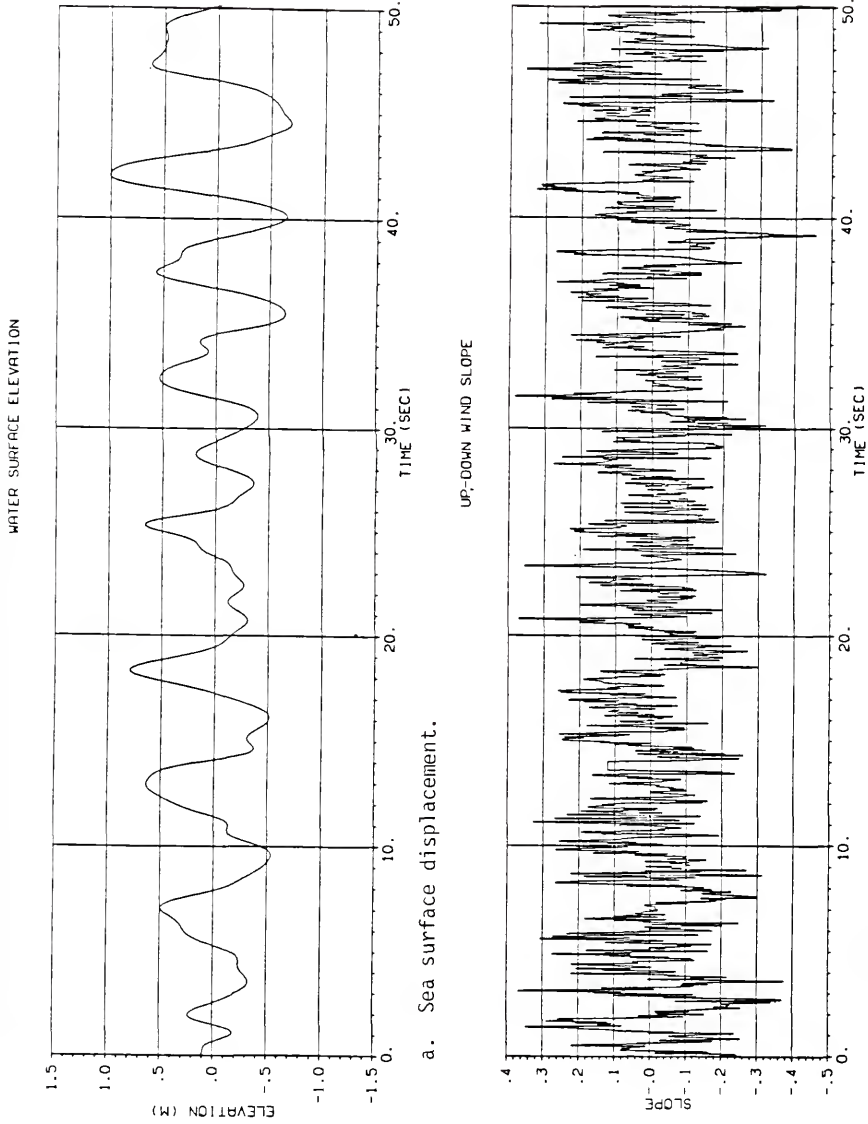


Fig. 11 Sample time series for sea surface displacement and slope for Run 108.

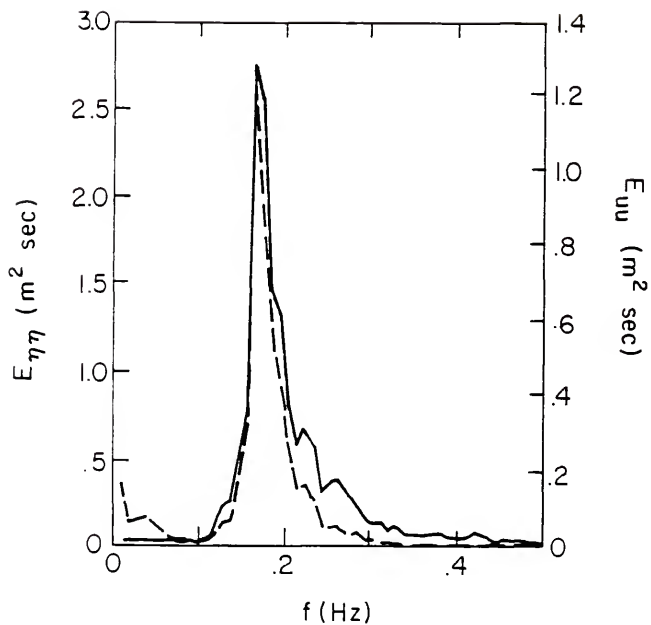


Fig. 12 Frequency spectra for η and u for Run 108. The solid line gives the surface displacement spectrum. The dashed line gives the u -component of the orbital velocity spectrum.

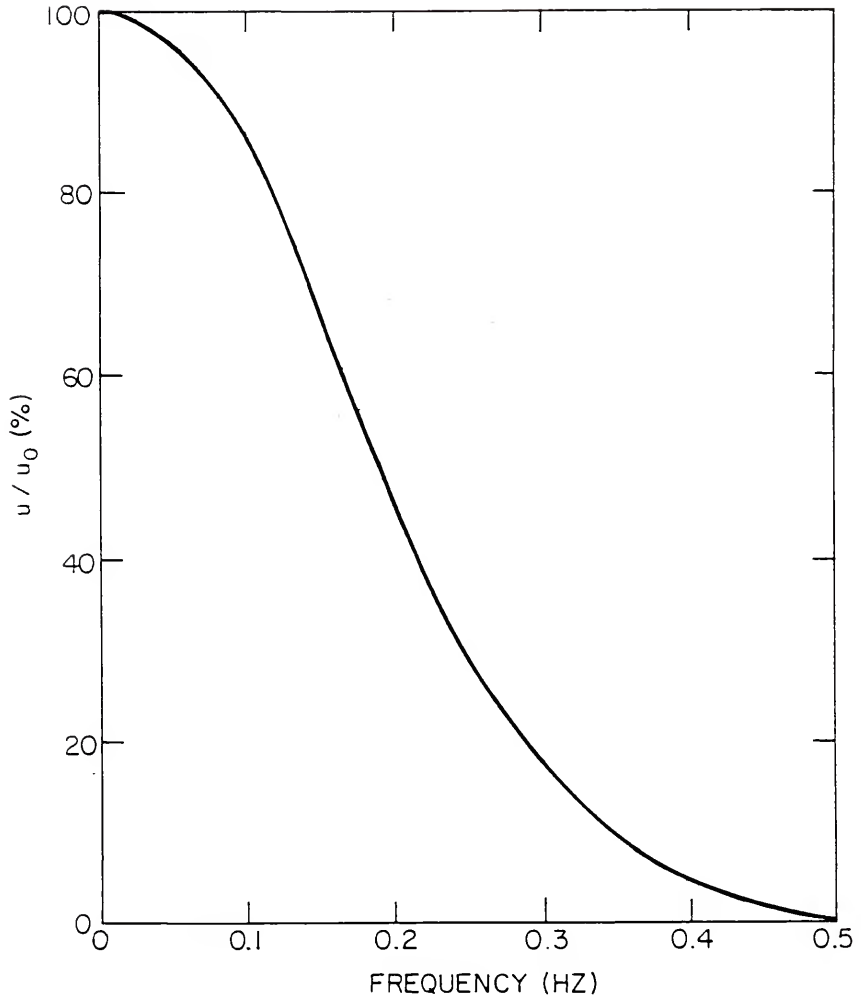


Fig. 13 Attenuation of the orbital velocity. u/u_0 is the ratio of u-component of orbital velocity at 4.75 m below the mean sea level to that at the sea surface.

The sampling rate for the current meter signal was set at 5 sps which was sufficiently high for wave frequencies less than 0.3 Hz.

The tidal current was considered as the D.C. component of each of the 15 min record lengths used. These values were compared favorably with those provided in Tidal Tables. A summary of the cases analyzed is given in Table 2. It is provided here as a guide for the subsequent analysis described in what follows.

The sea surface displacement signal is subject to inherent limitations due to the wave follower mechanical frequency response. The latter was found to be 1.0 Hz. The sea surface displacement time series were sampled at 25 sps. Because the current meter was stationed at 3.66 m away from the displacement sensor in the horizontal direction, a direct measure of the sea surface at the position of the optical sensor was not available. The method followed was to calculate the directional wave height spectrum from u , v and η time series and then to infer the surface orbital current at the location of the optical sensor. The latter was then used for demodulation analysis of surface wave slopes. The technique used for computing wave directional properties is described in Appendix A.

4.3 Determinations of Surface Wave Slope

Short wave amplitudes are small in nature; the slopes are tuned by the wavenumbers which are large for short waves. It is therefore easier to measure the slopes of short waves instead of their wave heights.

The laser-optical sensor was used to determine the surface normal \hat{n} as discussed before. The optical receiver used a photo-diode

Table 2
Observed Values of the Significant Wave Height,
Dominant Wind Direction and Tidal Current

Run ID	Wave Characteristics			Tidal Current	
	$H_{1/3}$ ⁽¹⁾ (m)	T_{peak} ⁽²⁾ (sec)	Direction of Dominant Wave ⁽³⁾ (degrees)	u_t (m/s)	θ_t ⁽³⁾ (degrees)
325	1.06	5.12	314	.16	247
326	1.05	5.39	332	.26	246
328	.59	5.69	310	.60	244
102	.45	5.39	238	.54	60
106	1.04	6.34	12	.72	51
107	1.59	7.88	347	.33	272
108	1.23	6.02	5	.29	217
217	.83	4.88	320	.35	238
104	.85	4.65	238	.60	36

- Note: (1) $H_{1/3}$ is the significant wave height
 (2) T_{peak} is the period of the spectral peak
 (3) true direction defined as before.

to determine the position of refracted laser beam. The latter was calibrated to give the coordinates in terms of γ and ϕ . For a fixed deflection angle, γ , the calibration voltages were recorded in the azimuth angle, ϕ , with increments of 45° . The procedure was repeated for deflection angles from 0° to 30° in increments of 5° .

Figures 14 and 15 show the calculated results after the application of the calibration curve derived from the best fit of the calibration signal for γ and ϕ . The rms errors were found to be 0.98° for γ and 5.7° for ϕ . Using equation (3.3), the slope component along a specified direction is determined. A sample of the down-wind slope is given in figure 11b. The corresponding slope spectrum (with EDF=100) is shown in figure 16. The probability density function derived in the standard procedure (Bendat and Piersol, 1971) is shown in figure 17.

4.4 Demodulation Analysis

As mentioned earlier, the encounter frequency of short waves deviates from the intrinsic frequency as the medium is swept by the orbital velocity of the long waves. The slope signals measured with the laser-optical sensor contain the Doppler effect due to wind drift, orbital velocity of long waves and tidal current. This Doppler effect must be removed in order to determine the dynamic properties of these modulated short waves. Removing the Doppler effect is referred to as "demodulation."

The demodulation procedure proposed by Evans and Shemdin (1980) was modified for this study. We first discuss the demodulation procedure used for the simple case of a monochromatic wave

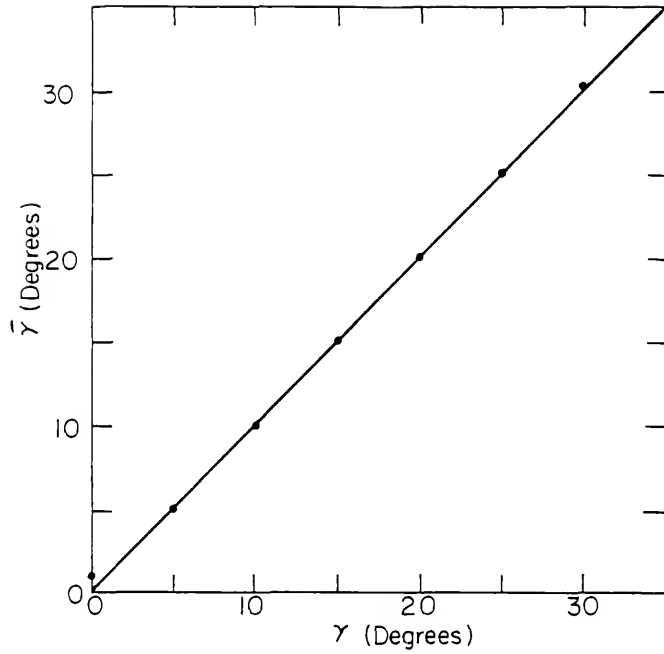


Fig. 14 Calibration results for the deflection angle; $\bar{\gamma}$ is the calculated value.

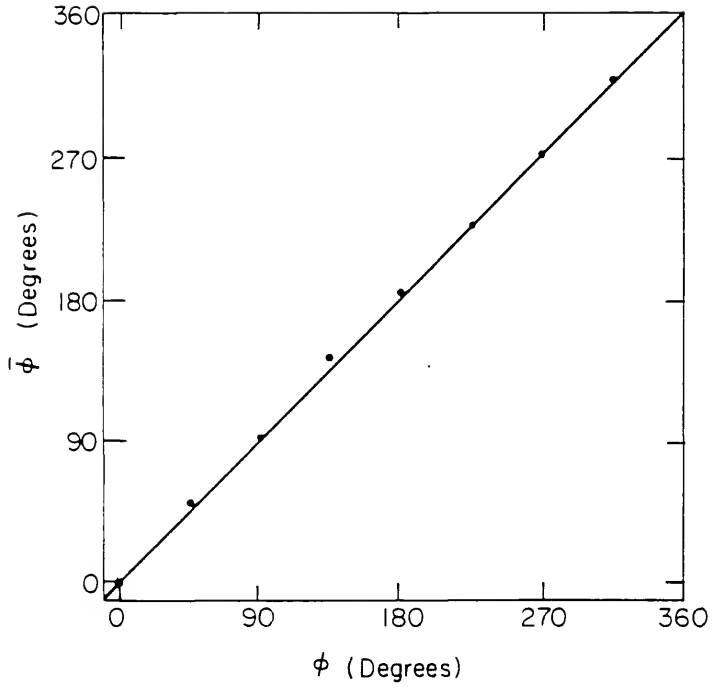


Fig. 15 Calibration results for the azimuth angle; $\bar{\phi}$ is the calculated value.

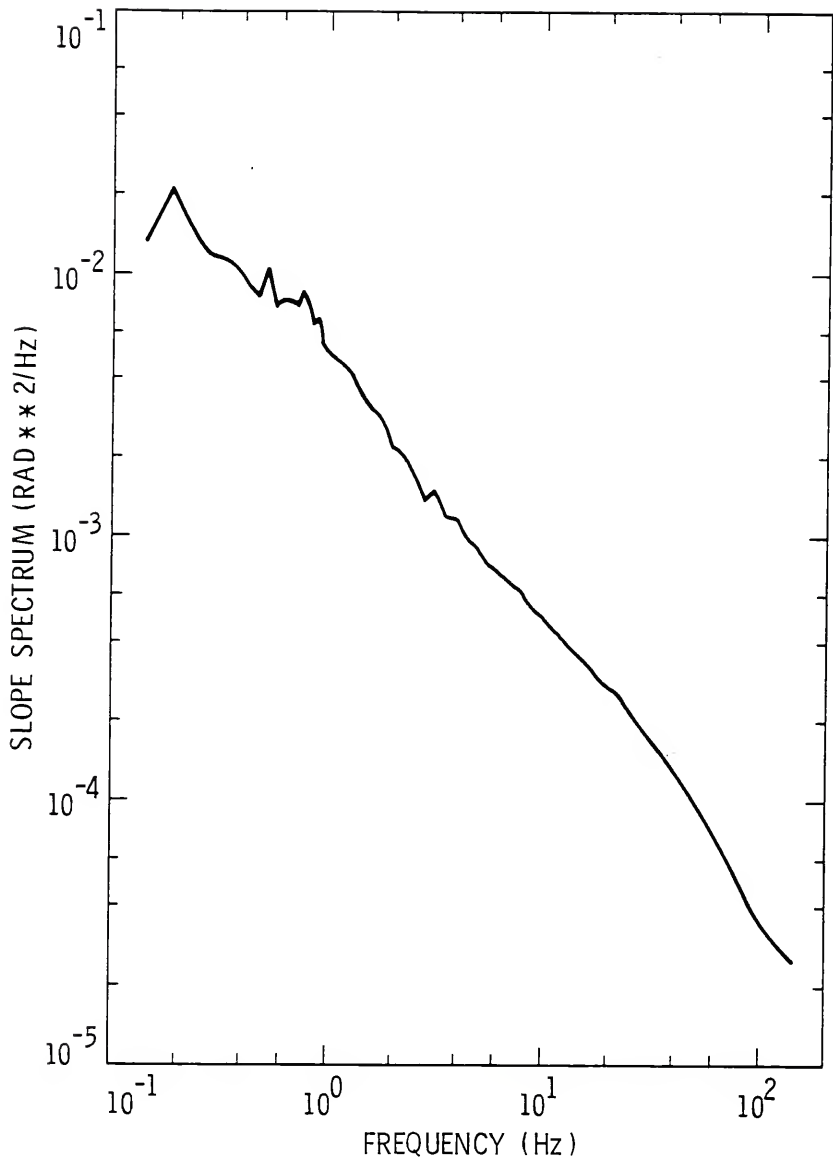


Fig. 16 The down-wind slope spectrum for Run 108; EDF = 100.

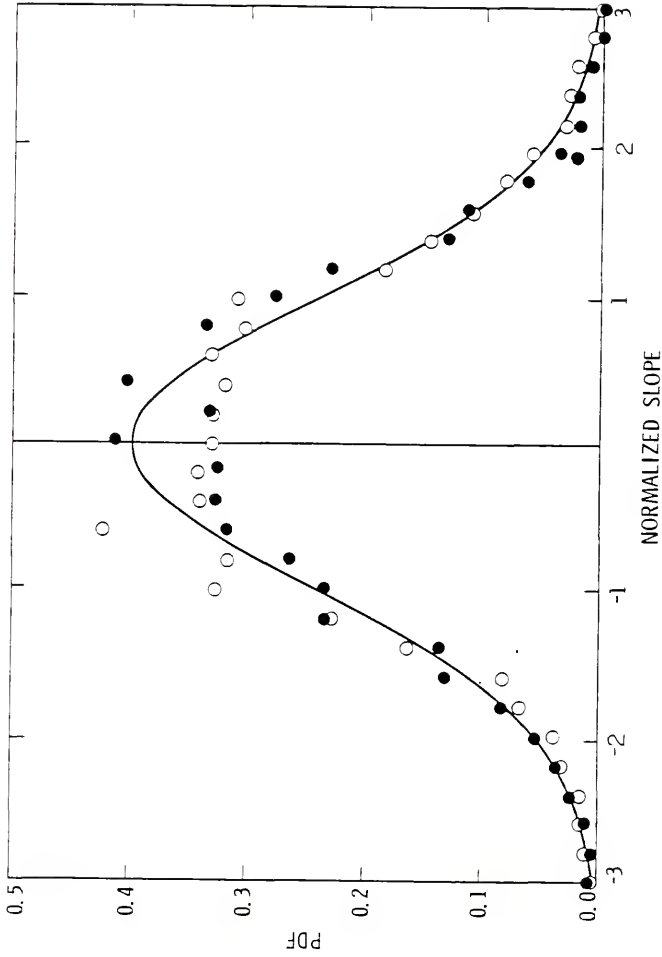


Fig. 17 Probability density function (PDF) of the sea surface slope summarized from 40,000 points of Run 103. The open circles and solid points denote the PDF for down-wind slope and the cross-wind slope, respectively. The normalized slope is the ratio of the slope to the standard deviation. The solid curve is a Gaussian distribution with the same variance. The variance of down-wind slope is 0.0342 and that of cross-wind slope is 0.0310.

train with direction θ , wave number k_λ and amplitude A_λ . The sea surface displacement at point (x_1, x_2) and time t is

$$\eta_\lambda(x_1, x_2, t) = A_\lambda \cos \left[(k_\lambda \cos \theta)x_1 + (k_\lambda \sin \theta)x_2 - \omega_\lambda t \right]. \quad (4.6)$$

The magnitude of the horizontal component of the surface orbital velocity at point $(0,0)$ can be approximated by

$$u_\lambda(0, 0, t) = u_\lambda(t) = \omega_\lambda \eta_\lambda \coth(k_\lambda h), \quad (4.7)$$

where h is water depth ($=18$ m), ω_λ is the radian frequency and k_λ is the wavenumber. The dispersion relation is given by

$$\omega_\lambda^2 = gk_\lambda \tanh k_\lambda h. \quad (4.8)$$

The medium travel speed along the direction of the short wave is given by

$$V_m = u_\lambda \cos \theta'_\lambda + u_t \cos \theta'_t, \quad (4.9)$$

where θ'_λ is the angle between the short wave and the long wave, θ'_t is the angle between the tidal current and the short wave.

The distance travelled by a short wave between two adjacent sample points is given by

$$\delta_x = |V_s + V_m| \cdot \Delta, \quad (4.10)$$

where V_s is the resultant phase speed and Δ is the sampling period. This relationship was found by Reece (1978) to be valid under laboratory conditions where the modulation of a wind-generated wave spectrum by a mechanically-generated monochromatic wave was investigated. Theoretical considerations of the interaction of

sinusoidal waves with current (Phillips, 1977) suggest that waves in an opposing current can only exist if

$$\sigma < g/4U_m ,$$

where σ is wave radian frequency in absence of current, g is gravitational acceleration and U_m is mean current. The results of Reece (1978) do not confirm this requirement suggesting that considerations based on monochromatic waves are not necessarily valid in wind-generated waves where the interaction of wind with a spectrum of waves plays the dominant role. Further evidence on this point is given by Wright (1976) who demonstrated experimentally that the induced wave breaking of short waves by long waves is different in character from that predicted by Banner and Phillips (1974) based on hydrodynamic considerations of monochromatic waves. While considerable research is in progress to provide insight on the interaction of wind generated short waves by long waves, the validity of equation (4.10) for the moment cannot be disputed. Hence, this equation is adopted for the demodulation analysis. It is recognized that the field conditions in MARSEN are different from the laboratory conditions from which this relationship was derived. The results derived from the demodulation analysis are therefore subject to the validity of equation (4.10) under field conditions.

In the presence of the wind, the resultant phase speed is given by Shemdin (1972)

$$V_s = C_s + \alpha U_a , \quad (4.11)$$

where C_s is the phase speed of the short waves given by

$$C_S = (g/k_S + \Gamma k_S / \rho)^{1/2} . \quad (4.12)$$

U_a is the wind speed, α is determined experimentally to be 0.03 (Huang, 1979). In equation (4.12) Γ is the sea surface-tension, and ρ is the sea water density. The gravitational acceleration in equation (4.12) is modified to give

$$g' = g - \omega_{\lambda}^2 \zeta_{\lambda}^2 , \quad (4.13)$$

where the second term on the right hand side is usually small under field conditions compared to the first and is neglected in this study. The demodulation procedure consists of computing an equivalent spatial distance for a given time series from equation (4.10). By using interpolation, a demodulated slope signal time series is derived in the spatial domain. The demodulated time series is then band-passed for a selected wavelength band in the wavenumber domain. The band-passed result is transformed back to time domain for cross-correlation with the surface displacement time series.

For the field data, the sea was composed of many sinusoidal waves. We assume that, for each frequency component, there is a dominant wave direction. We estimate the sea surface orbital velocity by summing u_{λ} calculated for each frequency component according to equation (4.7). The detail algorithm for demodulation is described in Appendix B.

Three wavelength bands were selected for demodulation. These were 3 cm, 8 cm and 23 cm which correspond to radar wavelengths for X, c and L band radars, respectively.

CHAPTER V EXPERIMENTAL RESULTS

Most of the accessory information for the runs is presented in Tables 1 and 2. The runs cover a range of wind speeds from 3.0 to 12.7 m/s. Figure 18 shows the sea surface displacement spectrum $E(f)$ where two peaks appear at two significantly different frequencies. The dominant peak of $E(f)$ at $f \approx 0.39$ Hz corresponds to the wind-generated wave, the secondary peak at $f \approx 0.19$ Hz corresponds to the swell. Cases like this will be identified as "mixed sea." In contrast, the sea surface displacement spectra shown in figures 19 and 20 represent "well-defined peak" cases and are typical of wind sea conditions. The sea conditions of the 12 runs are summarized in Table 3.

The principal results of this study are presented in various ways to bring out different points. We first present the general features of the wave slope spectra observed in the field. These will be followed by the results of the modulation of mean square slopes by long waves and the probability density function of wave slopes. The chapter is concluded by presentation of the calculated hydrodynamic modulation levels.

5.1 Characteristics of Wave Slope Spectra

Figure 21 illustrates the general features of the down-wind slope spectra at four different wind speeds from 3.5 m/s to 11.3 m/s.

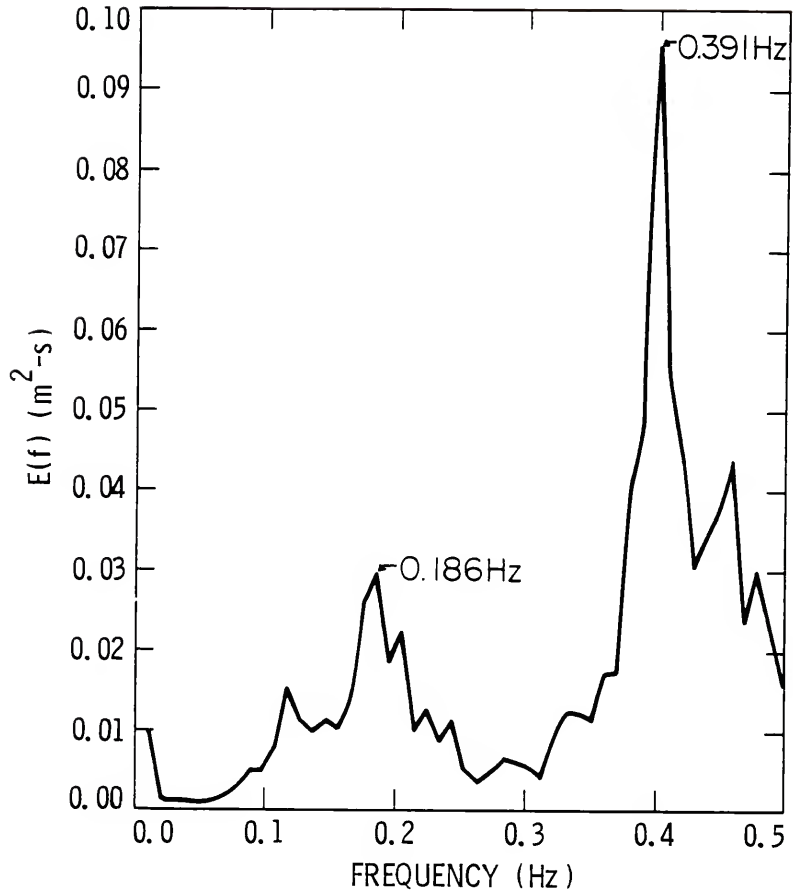


Fig. 18 An example of the sea surface displacement spectrum for "mixed sea" case. Run ID = 102, $U_a = 6.3$ m/s.

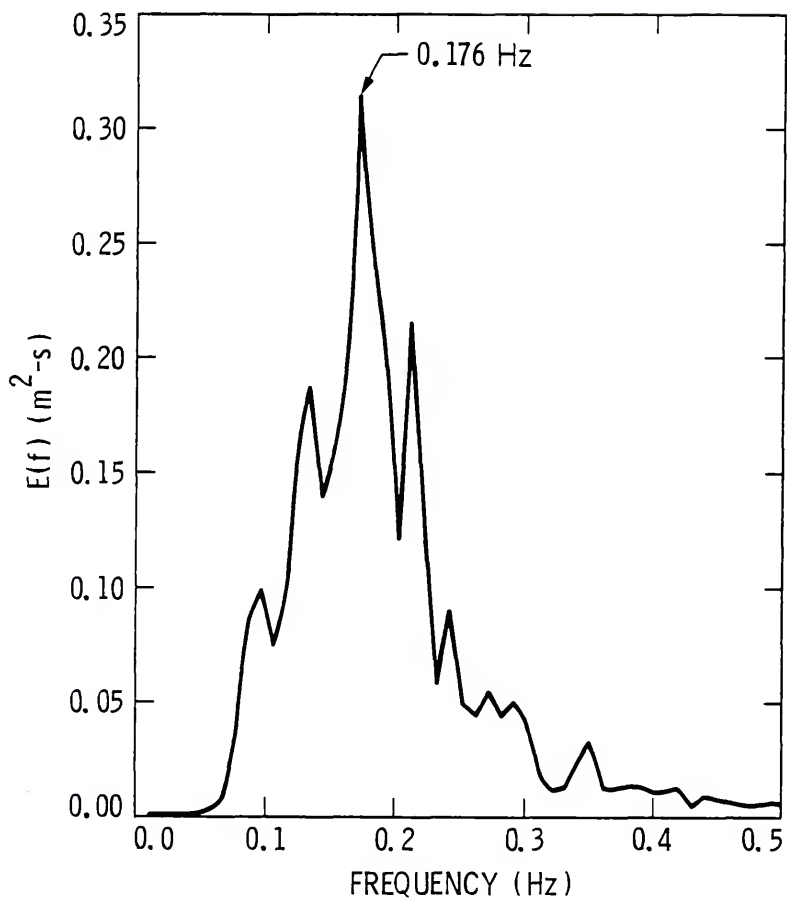


Fig. 19 Sea surface displacement spectrum of Run 328, a "well-defined peak" case. $U_a = 3.5$ m/s.

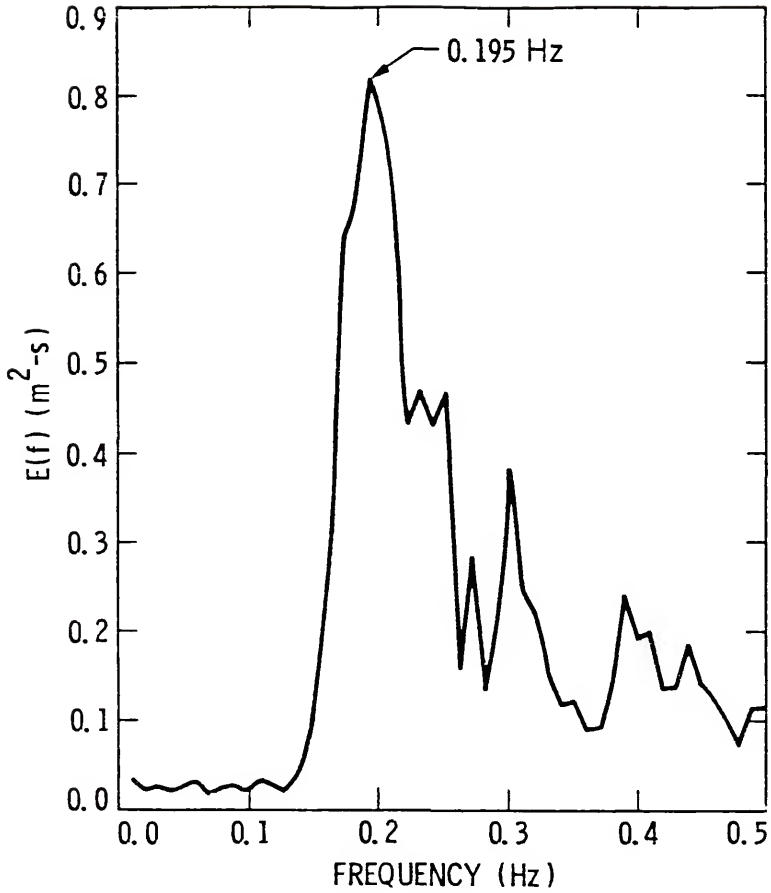


Fig. 20 Sea surface displacement spectrum of Run 325, a "well-defined peak" case. $U_a = 7.7$ m/s.

Table 3
Mean Square Wave Slopes and Sea Conditions

Run ID	U_a (m/s)	Mean Square Wave Slope		Sea Condition
		down-wind	cross-wind	
327	3.0	.0104	.0141	mixed sea
328	3.5	.0094	.0101	well-defined peak
110	4.3	.0223	.0209	mixed sea
217	4.5	.0259	.0189	mixed sea
104	5.0	.0309	.0382	mixed sea
107	5.4	.0447	.0429	mixed sea
106	5.9	.0347	.0267	mixed sea
102	6.3	.0098	.0117	mixed sea
326	7.5	.0218	.0317	well-defined peak
325	7.7	.0159	.0314	well-defined peak
108	11.3	.0342	.0310	well-defined peak
105	12.7	.0240	.0206	well-defined peak

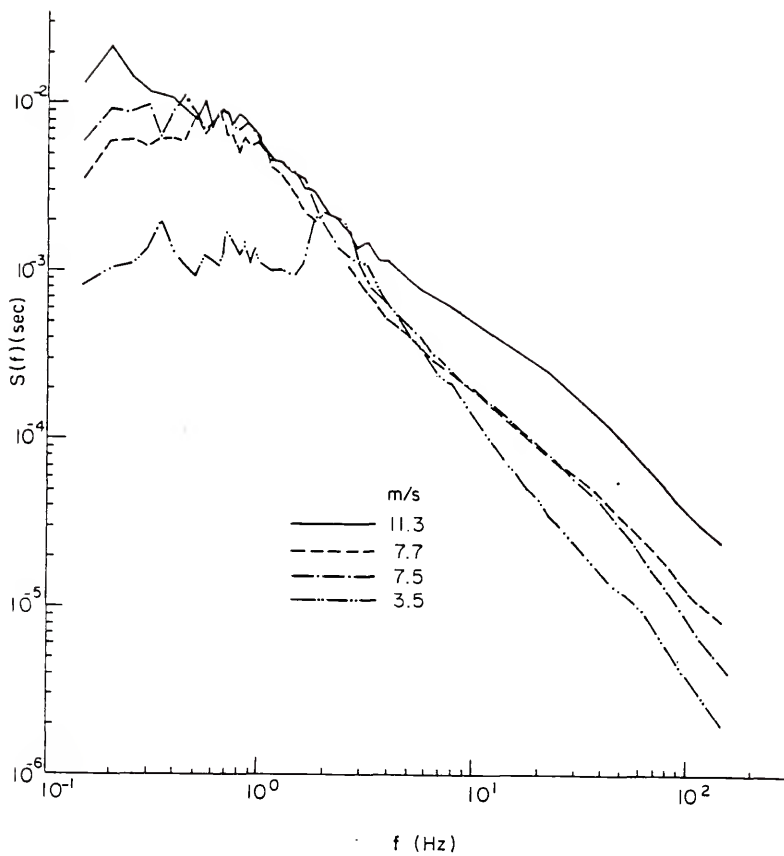


Fig. 21 The down-wind wave slope spectra.

The equivalent degrees of freedom (EDF) for each spectrum is 100; the Nyquist frequency is selected to be 200 Hz which is high enough to avoid the possible signal aliasing. Within the allowable error range, the wind dependence of the high frequency portion is evident. The frequency-weighted down-wind wave slope spectra for the same cases are shown in figure 22. It is noted that the shape of the spectrum varies from about $f^{-1.6}$ for low wind speed case to about f^{-1} for high wind speed case. The frequency-weighted down-wind wave slope spectrum normalized by that at the peak frequency is further illustrated in figure 23. It is expected that the high frequency part ($f/f_m > 1$) can be approximated by

$$\frac{f S(f)}{f_m S(f_m)} = \left(\frac{f}{f_m}\right) \tilde{F}(U_*) \quad (5.1)$$

where f_m is the peak frequency of the down-wind wave slope spectrum and the function $\tilde{F}(U_*)$ is to be determined from the shape of the down-wind wave slope spectrum. The air friction speed U_* is related to the wind speed U_a through the drag coefficient C_D , i.e.

$$U_*^2 = C_D U_a^2 \quad (5.2)$$

Figure 24 illustrates the best logarithmic fitted $\tilde{F}(U_*)$ for "well-defined peak" cases as

$$\tilde{F}(U_*) = 0.88 \log_{10}(U_*/42.5), \quad (5.3)$$

where U_* is in cm/s.

From the relation between the sea surface displacement spectrum and the wave slope spectrum in the gravity range

$$S(f) \approx f^4 E(f) \quad (5.4)$$

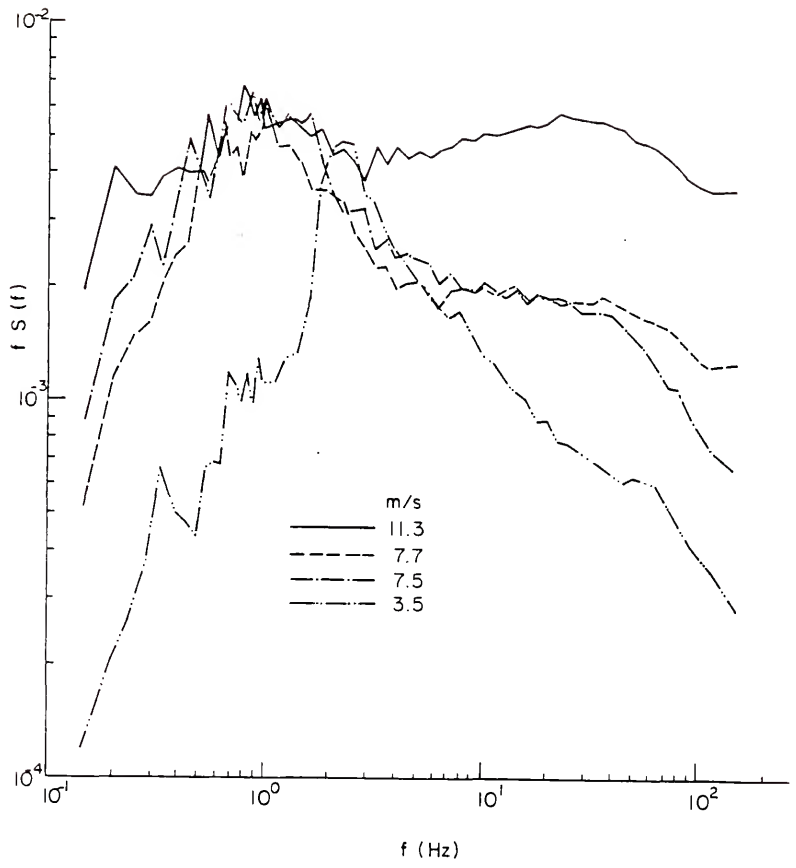


Fig. 22 The frequency-weighted down-wind wave slope spectra.

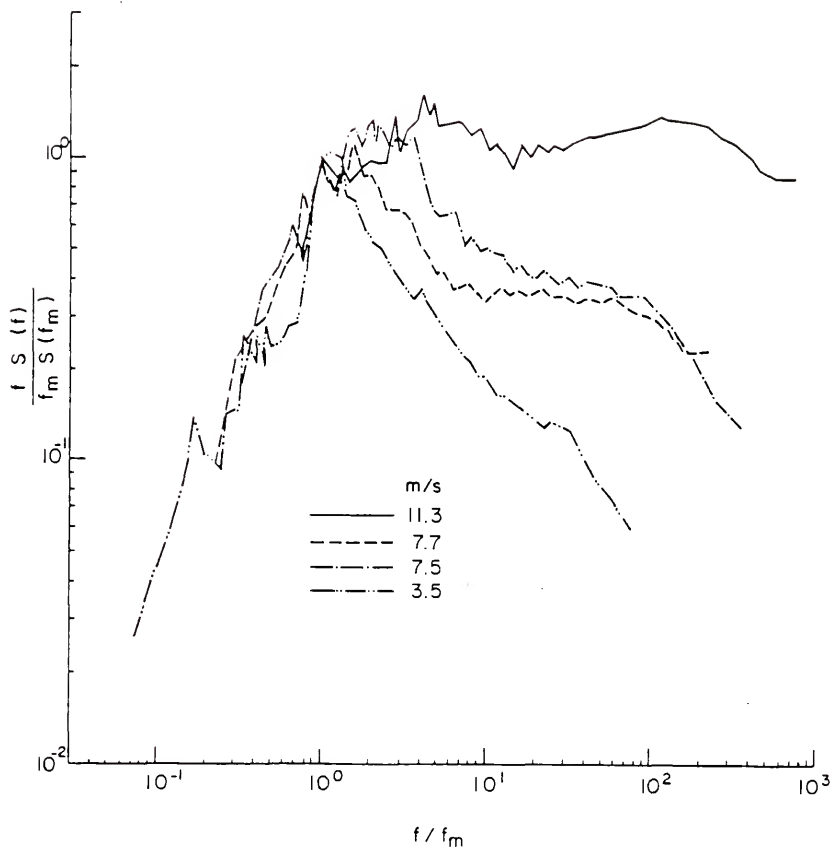


Fig. 23 The normalized down-wind wave slope spectra.

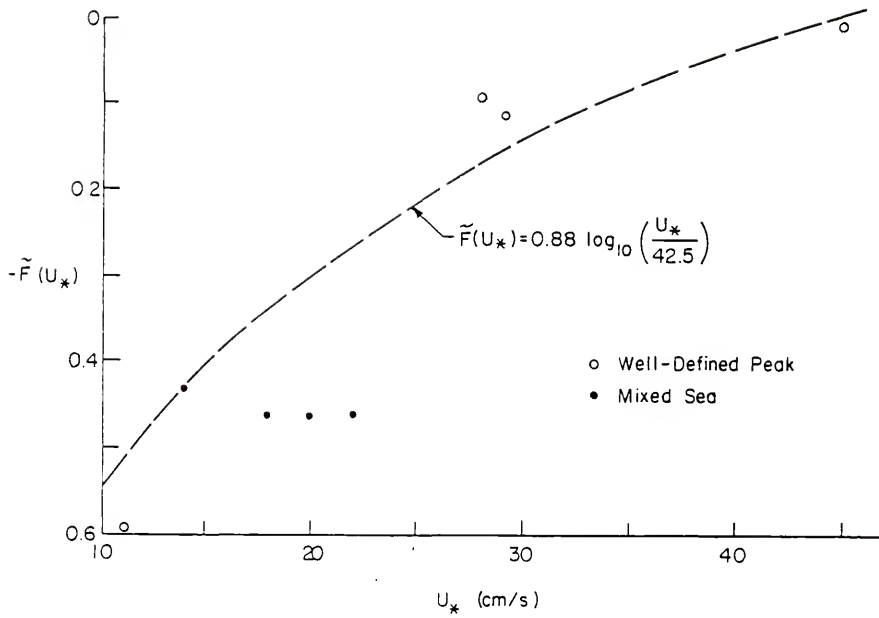


Fig. 24 Best fitted $\tilde{F}(U_*)$ from the cases of "well-defined peak."

Mitsuyasu and Honda's result (1974) shown in equation (2.2) can be reduced to

$$\frac{f S(f)}{f_m S(f_m)} = \left(\frac{f}{f_m}\right)^{\log_{10} U_*} \quad (5.5)$$

This is similar to our results shown in equation (5.1). Although the f^{-1} dependence in the wave slope spectrum is true for waves in the gravity and capillary ranges, the frequency dependence of that for waves in the capillary-gravity range is not clear. Furthermore, the dispersion relation of the high frequency wave is affected by the coexisting current and hence equation (5.4) is no longer valid in this situation. These can also account for the deviation from f^{-1} in our proposed spectral form shown in equation (5.1).

The mean square slopes for the down-wind and cross-wind components are presented in order of increasing wind speed in Table 3. The mean square wave slopes defined as the sum of the wave slopes along two orthogonal directions are illustrated in figure 25. It is noted that "mixed-sea" cases show high values of the mean square wave slopes. All "well-defined peak" cases except one associated with oil-slick experiment ($U_a = 12.8$ m/s) show increasing mean square wave slopes with higher wind speeds.

5.2 Modulation of Mean Square Wave Slopes by Long Waves

To investigate the modulation of the wave slope signal by long waves, we first calculate the cross-correlation function $\tilde{C}(\tau)$ of the local mean square down-wind wave slopes, s^2 , and the sea surface displacement η from the equation

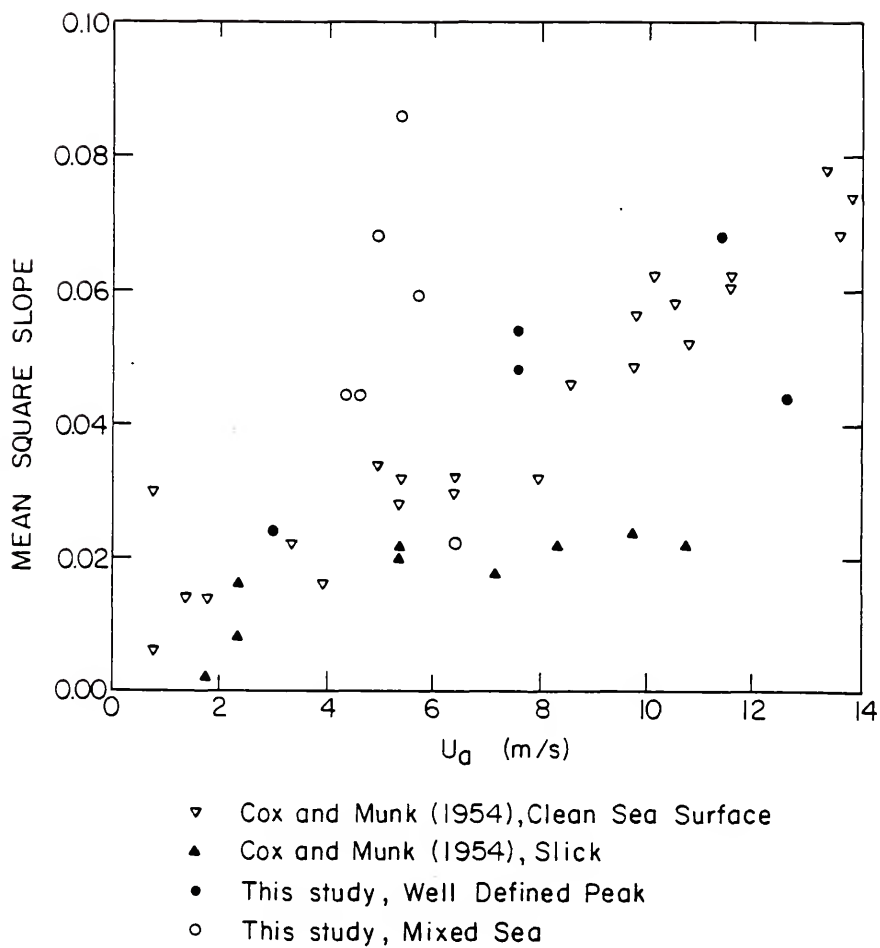


Fig. 25 Mean square wave slope as a function of the wind speed.

$$\tilde{C}(\tau) = \frac{1}{T} \int_0^T s^2(t) \eta(t+\tau) dt \quad , \quad (5.6)$$

where $T (= 327.68 \text{ sec})$ is the averaging period. An example of the cross-correlogram is shown in figure 26. The periodic feature shown in the figure is typical for all cases studied.

The phase lead θ_{\max} in degrees is calculated by

$$\theta_{\max} = \frac{\tau_{\max}}{T_{\text{peak}}} \times 360^\circ \quad (5.7)$$

where τ_{\max} is the lag of the first peak in the cross-correlogram, T_{peak} is the peak period of the waves. It is interesting to note that θ_{\max} is a function of wind speed as shown in figure 27. The normalized cross-correlation function, defined as the cross-correlation function normalized by the product of the standard deviation of local mean square down-wind wave slope and that of sea surface displacement, gives the strength of correlation for each case. The peak values of the normalized cross-correlation function, $\tilde{\rho}_{\max}$, are plotted against the wind speeds in figure 28. Neither "well-defined peak" cases nor "mixed sea" cases show any significant trend.

5.3 Probability Density Function of Wave Slopes

The probability density functions for down-wind and cross-wind wave slopes are calculated from 40,000 data points. Figures 17, 29 and 30 show the probability density functions of "well-defined peak" cases at various wind speeds. Figure 31 illustrates a probability density function in a "mixed sea" case.

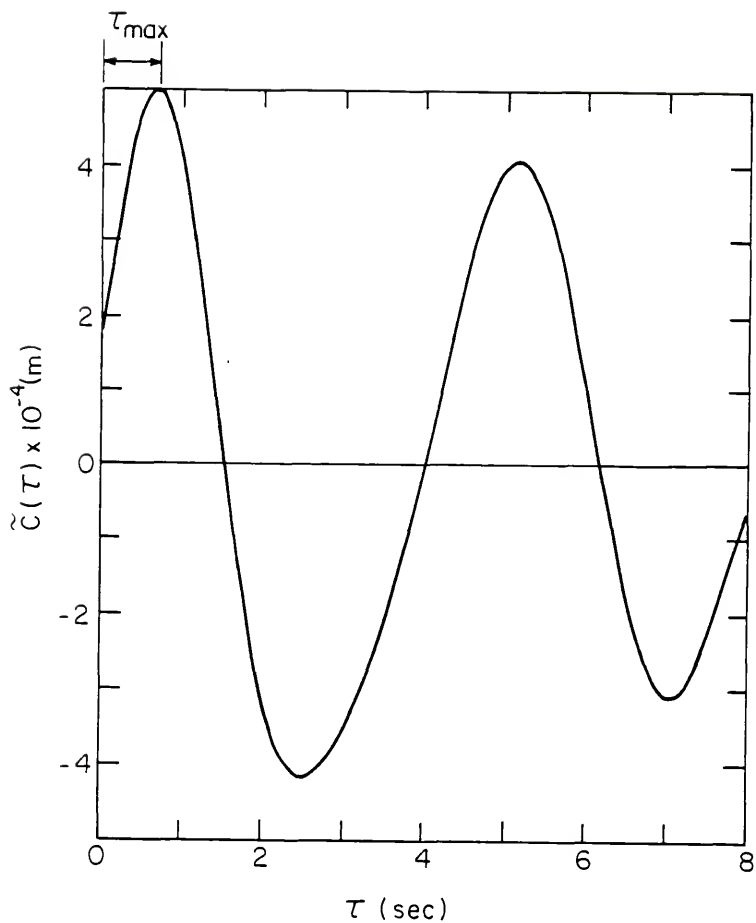


Fig. 26 The cross-correlation function of mean square down-wind wave slope and sea surface displacement for Run 325. The lag of the first peak in the cross-correlation defines τ_{max} .

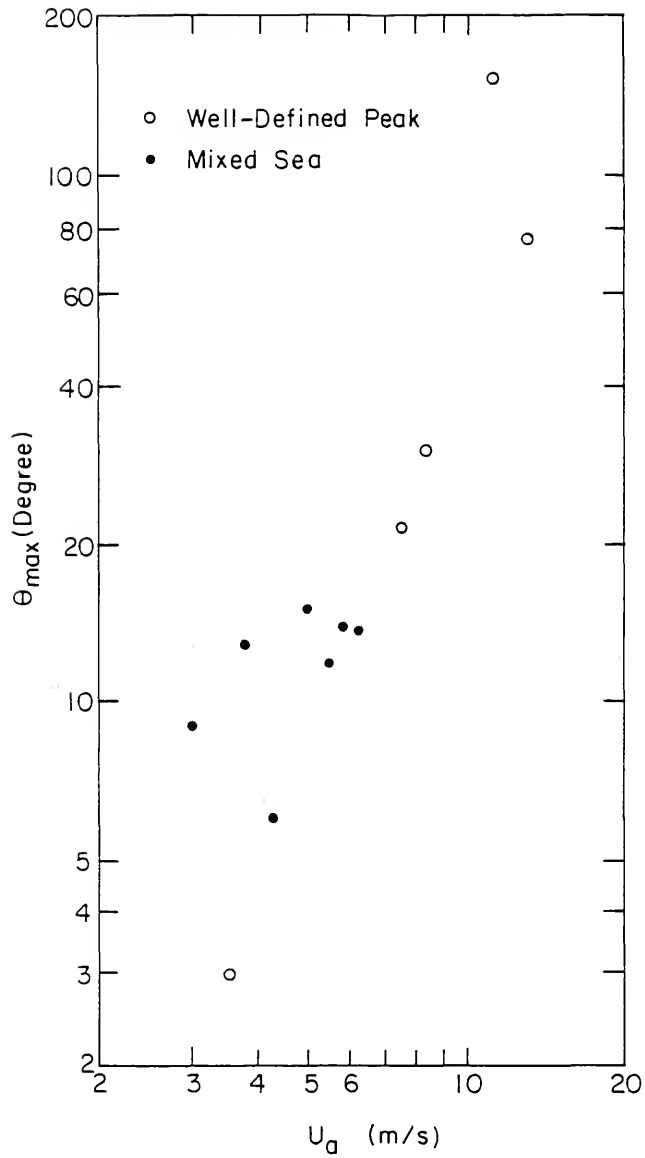


Fig. 27 The phase lead θ_{max} as a function of wind speed U_a .

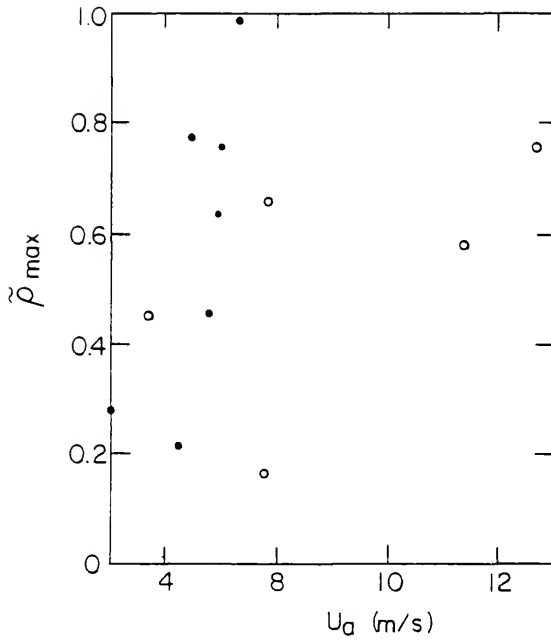


Fig. 28 Peak value of the normalized cross-correlation function as a function of wind speed. The open circles and solid points denote $\tilde{\rho}_{\max}$ values of "well-defined peak" cases and "mixed-sea" cases, respectively.

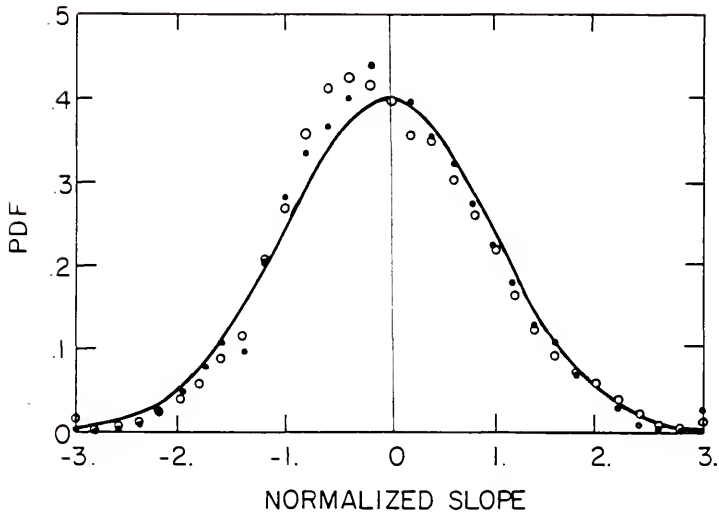


Fig. 29 Probability density function for Run 328. The notation used is the same as that in figure 17; $U_a = 3.5$ m/s; the variances are 0.0094 for down-wind wave slopes^a and 0.0101 for up-wind wave slopes.

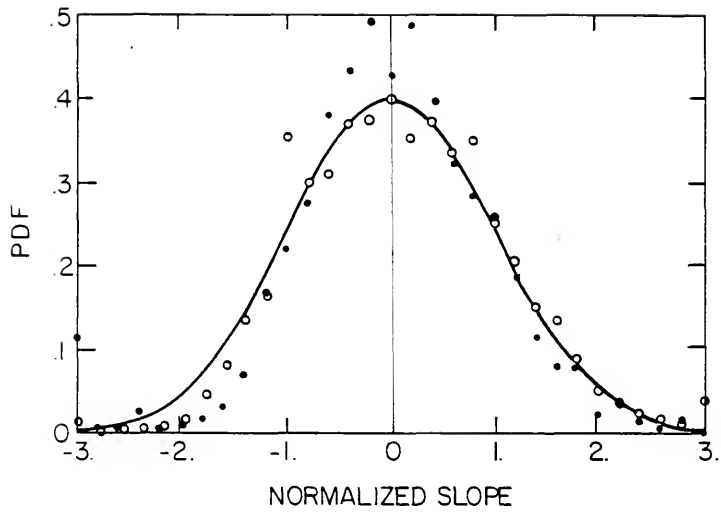


Fig. 30 Probability density function for Run 325. The notation used is the same as that in figure 17; $U_a = 7.7$ m/s; the variances are 0.0159 for down-wind wave slopes and 0.0314 for cross-wind wave slopes.

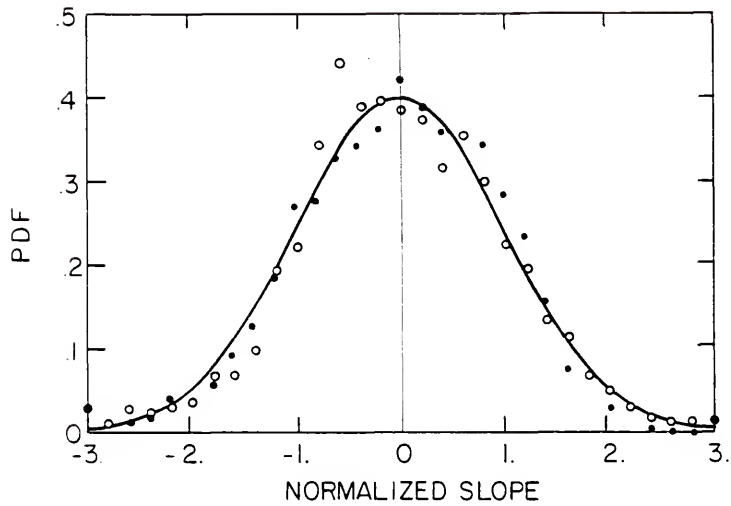


Fig. 31 Probability density function for Run 102. The notation used is the same as that in figure 17; $U_a = 6.3$ m/s; the variances are 0.0098 for down-wind slopes and 0.0117 for cross-wind slopes.

All cases show similar distributions; cross-wind slopes are relatively peaked at the origin compared to the down-wind slope distributions. The down-wind slope distribution does not show obvious skewness in the windward direction; this is not consistent with the observations by Cox and Munk (1954). In contrast, some cases reveal (figures 17, 30 and 31) double peaks in the down-wind probability density functions.

5.4 Modulation of Short Waves by Long Waves

To study the radar imaging mechanism, we need to investigate the hydrodynamic modulation level for a particular wavelength band. This work was done by carrying out the cross-correlation analysis on the demodulated short wave signals and the sea surface displacement.

Table 4 illustrates the general characteristics of the short wavelength bands elected for the modulation study.

If we compare equation (2.31) with equation (2.35), we have the following analogies between measurements of hydrodynamic modulation and those of radar modulation:

<u>Radar Modulation</u>	<u>Hydrodynamic Modulation</u>
p	F
\bar{p}	$F(0)$
\tilde{v}	η
M_{radar}	M

Because the line of sight speed \tilde{v} is of the same order as $\sigma_{\lambda} \eta$ and the short wave energy density is proportioned to the short wave slope square. Equation (2.36) can be generalized to

Table 4
The Wavelength Bands for Modulation Study

Lower bound λ_- (cm)	Upper bound λ_+ (cm)	$\lambda_S = \frac{(\lambda_+ + \lambda_-)}{2}$	f_S (Hz)	B(1) (%)	B(2) (%)	Radar band with wavelength λ_S	Radar frequency (Giga Hz)
2	4	3	8.3	33	33	X	10.00
5	11	8	4.5	4	4	c	3.75
18	28	23	2.6	0.5	0.5	L	1.30

$$(1) (2\pi f_S)^2 = gk_S + \frac{\Gamma k_S^3}{\rho}, \text{ where } k_S = 2\pi/\lambda_S, g = 9.8 \text{ m/s}^2, \Gamma = 0.072 \text{ kg/s and } \rho = 10^3 \text{ kg/m}^3.$$

(2) B is the Bond (or Weber) number characterizing the relative weight of the surface tension to that of the gravity; $B = \Gamma k_S^2 / g\rho$.

$$M = \frac{1}{s^2 k_\lambda} \frac{E_{S^2\eta}}{E_{\eta\eta}} \quad (5.8)$$

where $E_{S^2\eta}$ is the cross-spectrum of the demodulated mean square slope signal and the sea surface displacement, $E_{\eta\eta}$ is the auto-spectrum of the latter and k_λ is the long wavenumber.

Figures 32 to 34 illustrate the hydrodynamic modulation levels of the three wavelength bands selected at three different wind speeds. It is noted here that the hydrodynamic modulation level is the lowest for the 8 cm wave at the lowest wind speed. The wind-dependence for various wavelength bands is shown in figures 35 to 37. The most striking feature is that the lower the mean wind speed the higher the modulation level for each wavelength band.

The modulation level for one "mixed sea" case, shown in figure 38, shows much higher values than those in "well-defined peak" cases under similar wind speed conditions.

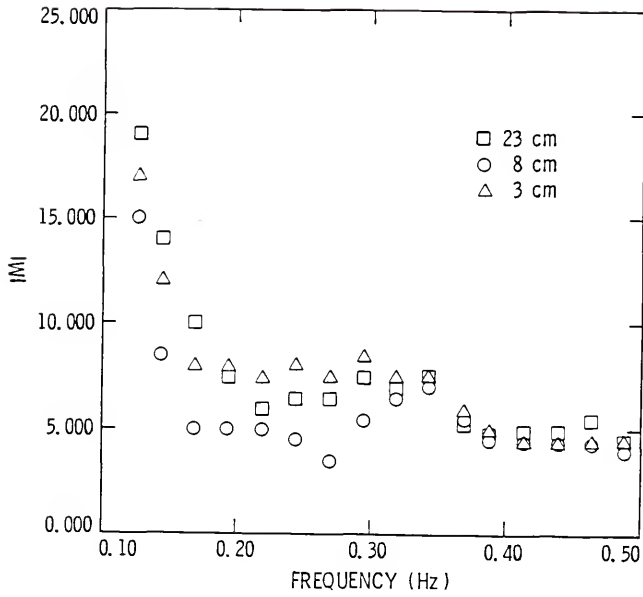


Fig. 32 Hydrodynamic modulation level for Run 328. $U_a = 3.5$ m/s.

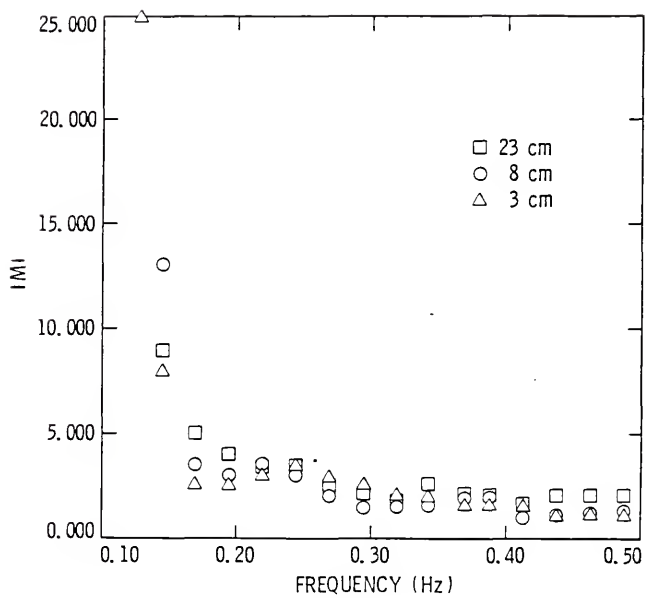


Fig. 33 Hydrodynamic modulation level for Run 325. $U_a = 7.7$ m/s.

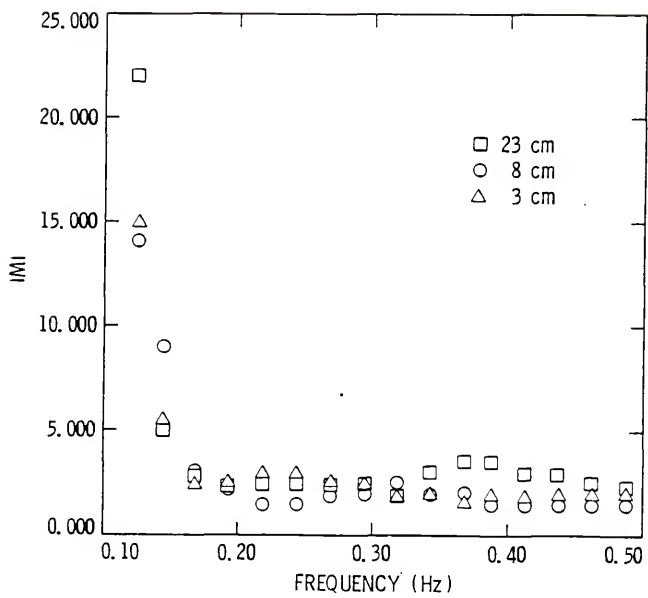


Fig. 34 Hydrodynamic modulation level for Run 108. $U_a = 11.3$ m/s.

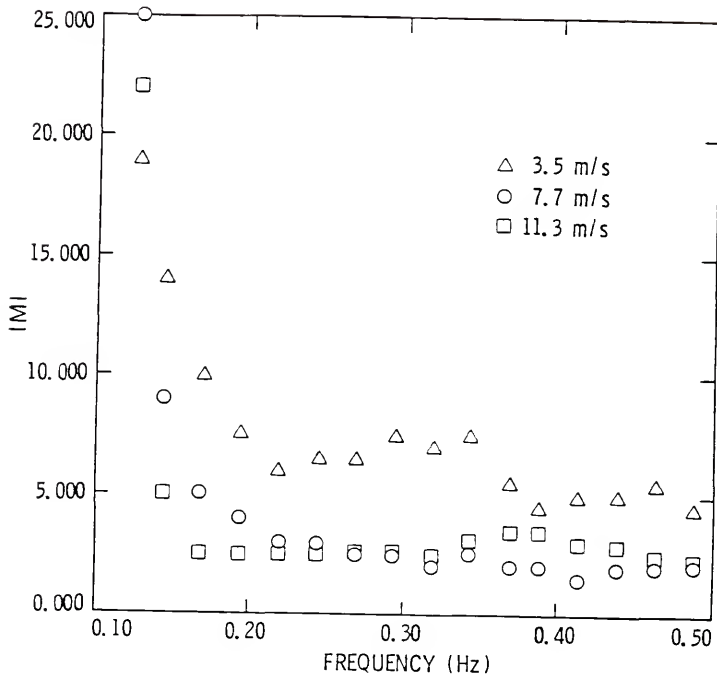


Fig. 35 Hydrodynamic modulation level for 23 cm waves.

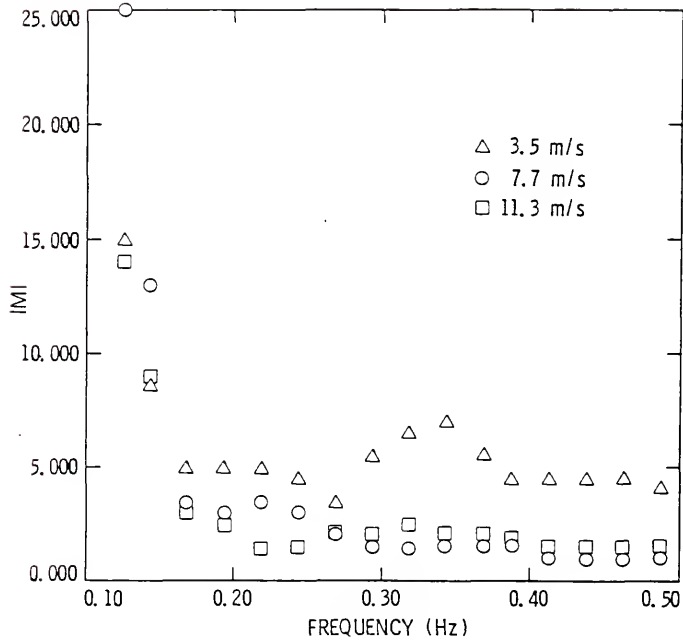


Fig. 36 Hydrodynamic modulation level for 8 cm waves.

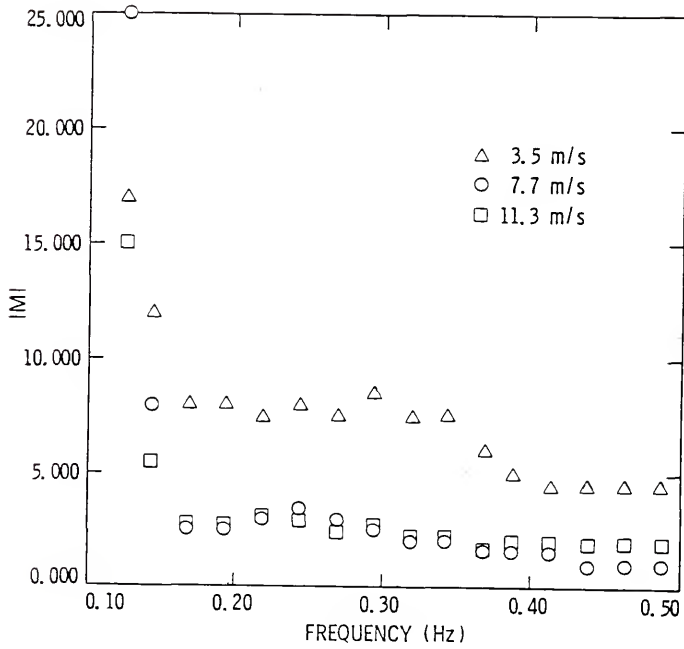


Fig. 37 Hydrodynamic modulation level for 3 cm waves.

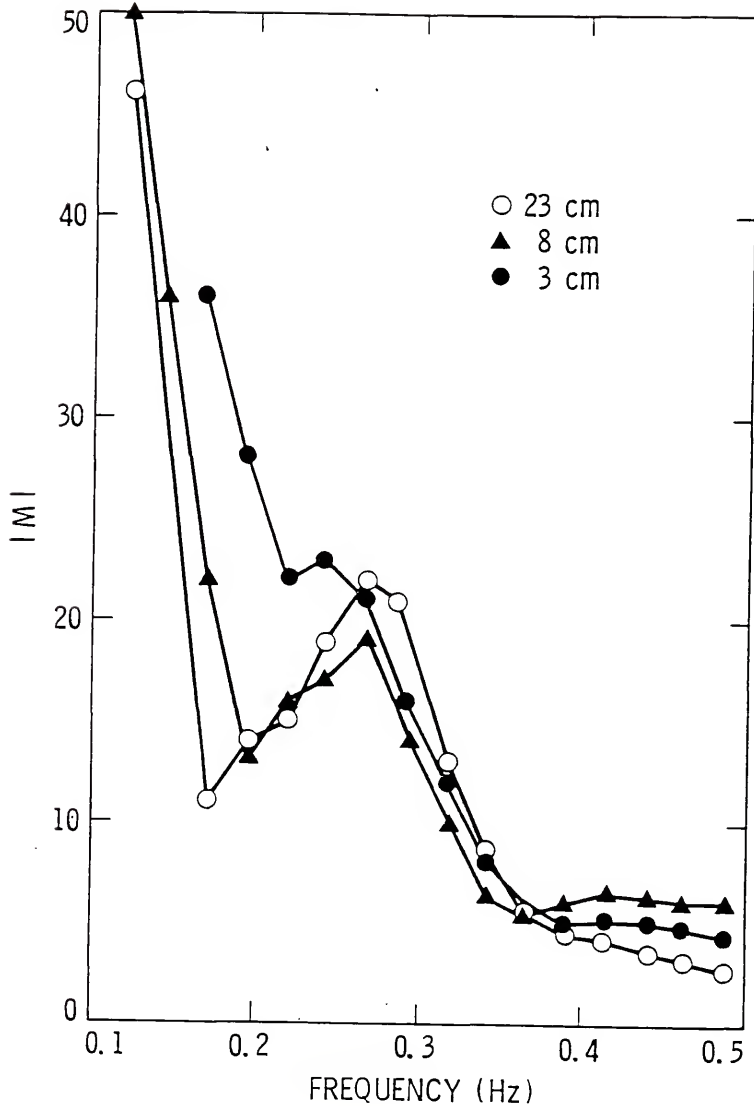


Fig. 38 Hydrodynamic modulation level for a "mixed-sea" case.
Run ID = 102, $U_a = 6.3$ m/s.

CHAPTER VI DISCUSSION OF RESULTS

The results presented in the previous chapter are scarce in company. Besides the observation of Cox and Munk (1954) and those of Evans and Shemdin (1980) we know of no other direct field measurements of wave slopes. In fact, this study is the only in situ field investigation of the hydrodynamic modulation in a two dimensional wave field.

6.1 Wave Slope Spectra

The principal finding from the down-wind wave slope spectra is the dependence of high frequency waves on wind speed. Under laboratory conditions the wind speed dependence of the down-wind slope spectrum is reported by various investigators, the last being Lleonart and Blackman (1980). The conclusions derived from the laboratory experiments all support a f^{-1} law for high frequency waves (equation (2.5)). The same investigation does not provide converging views on the wind dependence of the high frequency waves as stated in section 2.2. The proposed spectral form shown in equation (5.1) is seen to agree well with the spectral form (equation (5.5)) suggested by Mitsuyasu and Honda.

The mean square wave slopes measured by Cox and Munk (1954) from sun glitter have compared with our results, as shown in figure 25. All "well-defined peak" cases show the same trend as those reported by Cox and Munk. The results from the "well-defined peak" cases fall

within the limit of data scatter and in agreement with those of Cox and Munk. The "mixed sea" cases show mean squared slopes that are higher than those of "well-defined peak" cases and those of Cox and Munk. This peculiar behavior is currently under further investigation.

6.2 Modulation of Mean Square Wave Slopes

The modulation of mean square slopes is measured by the cross-correlation of the mean square wave slope and sea surface displacement as shown in equation (5.6). The cross-correlogram reveals the presence of the dominant frequency which is close to that at the peak of the surface displacement spectrum. This result suggests that our assumption of the cyclic change in the energy spectrum made in equation (2.29) is reasonable.

The local mean square slope leads the long wave with the angle θ_{\max} varying from 3° to 150° with wind speeds varying from 3.0 m/s to 12.7 m/s. Evans and Shemdin (1980) reported θ_{\max} to vary from 30° to 45° with a wind speed $U_a = 5 \pm 1$ m/s. Our θ_{\max} suggests a strong variation of θ_{\max} with U_a .

When the radar incidence angle is small ($\leq 20^{\circ}$), the radar backscatter is from the entire wave spectrum rather than from the Bragg waves only (Valenzuela, 1978). Our cross-correlation analysis presented here should be useful for determining radar modulation at such small incidence angles. The normalized cross-correlation function which gives the relative strength shows no evidence of dependence on wind speed (see figure 28).

6.3 Probability Density Function

All the probability density functions computed are found to follow the Gaussian distributions; this is consistent with Wu's laboratory results (1971). The cross-wind wave slope distribution is slightly peaked, this follows the field observation by Cox and Munk (1954).

However, the double peak in the probability density function of down-wind wave slopes (see figures 17, 30 and 31) might be caused by the peak downward profile of capillary waves as noted by Schooley (1958). The field investigation by Cox and Munk (1954) from sun glitter probably averaged out these fine scale features of waves.

6.4 Hydrodynamic Modulation Level

Few direct measurements of the short wave modulation by long waves have been made in the field. In fact this is the first attempt to investigate the short wave slope modulation in a two-dimensional field setting. The only comparable measurements are those of Wright et al. (1978) who used frequency modulations of backscattered microwaves to obtain the wave orbital speed and backscattered power modulation to obtain the amplitude modulation of the (short) scattering waves. By using the optical sensor and other supporting measurements, it is hoped that the actual hydrodynamic modulation levels can be measured directly rather than inferred from radar backscatter.

The maximum modulation level predicted from the relaxation model is $-(k_s/F^{(0)})(\partial F^{(0)}/\partial k_s) + \gamma_1$ which is higher for the steeper spectral shape. The modulation levels shown in figures 32 to 34 with values 3 to 25 are larger than $-(k_s/F^{(0)})(\partial F^{(0)}/\partial k_s) + \gamma_1$ in general. However, the

wind speed dependence of the modulation level illustrated in figures 35 to 37 agrees well through the inference of the relaxation model and the wind speed dependence on the spectral shape (section 5.1). That is the lower the wind speed, where the down-wind slope spectral shape is steeper, the higher the modulation level as predicted from the relaxation model.

The power dependence of the high wavenumber (frequency) energy spectrum will make $(k_s/F^{(0)})(\partial F^{(0)}/\partial k_s)$ independent from the wavenumber of the short wave and therefore, according to the relaxation model, the modulation level is independent of the selected wavelength band. Our results show that the modulation levels for 3, 8 and 23 cm waves are of the same order.

Similar to the radar modulation transfer function reported by Wright et al. (1980), the increase in the modulation level with decreasing wave frequency is opposite to that predicted by the relaxation model if the relaxation rate is assumed constant.

Figures 39 to 41 show comparisons of the hydrodynamic modulation levels for 8 cm and 23 cm waves with the modulus of the radar transfer function for X band ($\lambda_r = 2.3$ cm) and L band ($\lambda_r = 23$ cm) radars. The hydrodynamic modulation level, $|M|$, is smaller than the modulus of radar modulation transfer function, $|M_{\text{radar}}|$. The radar modulation transfer function measured by Wright et al. includes the possible scattering effect of the intermittent breaking of short waves when they are saturated at the long wave crest. Our wave follower measurement, due to the inherent restrictions, averaged out this fine scale wave breaking. Further studies are needed to investigate the contribution of the small wave breaking on the radar backscatter.

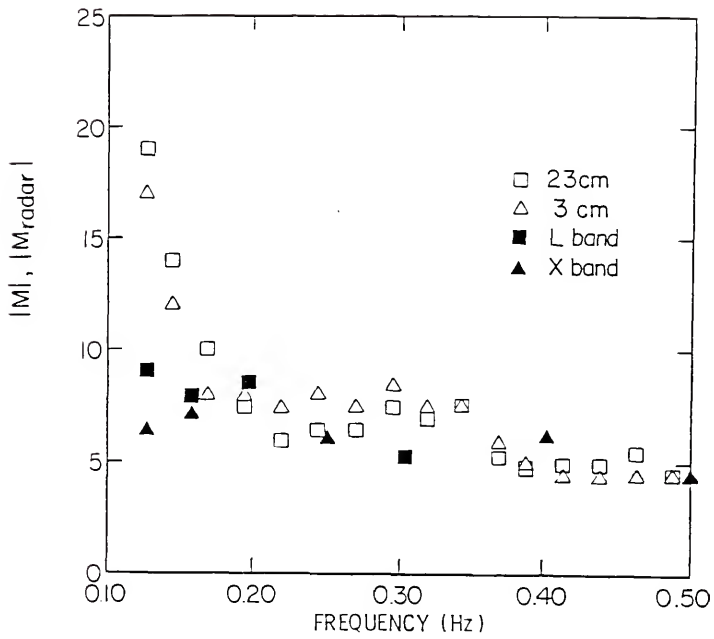


Fig. 39 Comparison of hydrodynamic modulation level and modulus of radar modulation transfer function for $U_a = 3.5$ m/s.

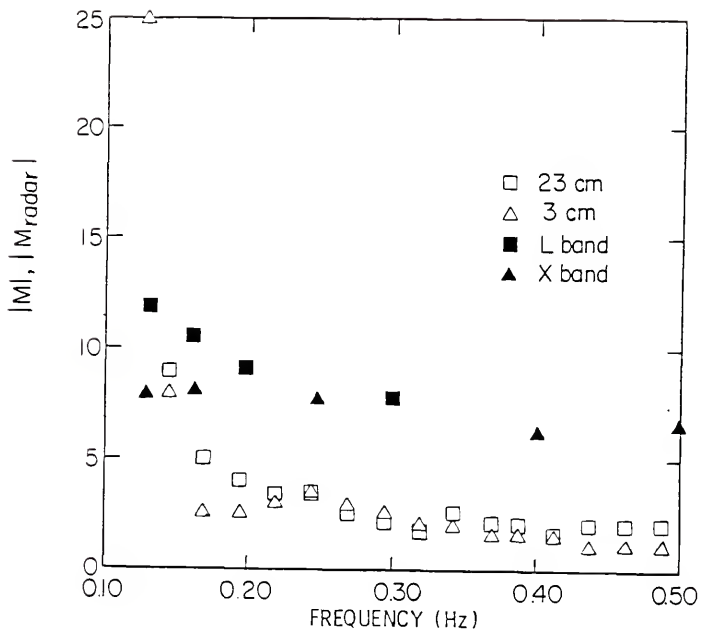


Fig. 40 Comparison of hydrodynamic modulation level and modulus of radar modulation transfer function for $U_a = 7.7$ m/s.

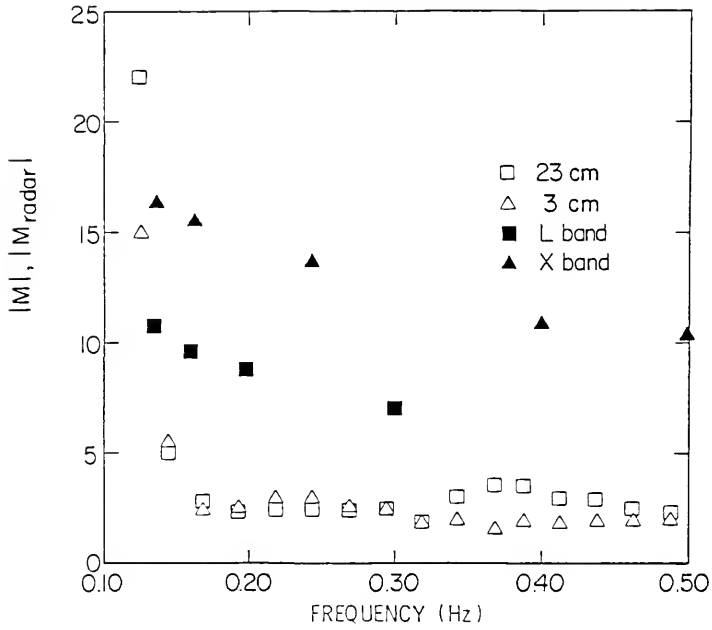


Fig. 41 Comparison of hydrodynamic modulation level and modulus of radar modulation transfer function for $U_a = 11.3$ m/s.

At the low wind speed (figure 29) $|M|$ and $|M_{\text{radar}}|$ are of the same orders; this implies that hydrodynamic modulation is strong enough to constitute a major radar imaging mechanism for ocean waves.

CHAPTER VII
CONCLUSIONS AND RECOMMENDATIONS

7.1 Conclusions

The cases investigated in this study covered a wind speed range from 3.0 m/s to 12.7 m/s. Within this range the important conclusions are reported below.

- (i) The slope of the high frequency region of the normalized down-wind wave slope spectrum is wind-speed dependent.
- (ii) Mean square wave slopes in the "well-defined peak" cases are consistent with observations reported by Cox and Munk (1954). However, the mean square slopes from the "mixed sea" cases show higher values than those observed by Cox and Munk (1954).
- (iii) The mean square down-wind slope, which is proportional to the short wave energy, reveals a modulation induced by the dominant long wave. The phase lead of this modulation, relative to the dominant long waves, increases with the wind speed.
- (iv) The hydrodynamic modulation level, obtained by the demodulation technique, decreases with the increasing wind speed. This tendency is consistent with the relaxation model results (Keller and Wright, 1975).
- (v) The measured hydrodynamic modulation magnitudes are of the same order as the radar modulation transfer function for

the low wind cases, the former are smaller than the latter for the high wind speed cases. This implies that the hydrodynamic modulation at low wind speeds is strong enough to constitute an important mechanism in radar imaging of ocean waves.

- (vi) The decreasing trend of the hydrodynamic modulation level with increasing wave frequency agrees with radar modulation transfer function results.

7.2 Recommendations

Future work in the line of the present research is described as follows:

- (i) In this experiment the laser-optical sensor is the sole instrument that provides the wave slope components along two specified directions. Slope components thus obtained could be contributed by waves coming from other directions. To make more direct comparison with the data measured by radar which only responds to the ocean wave coming from one particular direction, it is required to design a hardware system that is capable of detecting the directional properties of short waves.
- (ii) Although the demodulation procedure developed in this dissertation is complete in its present form, alternative analyses can be pursued conveniently in the frequency domain. However, the high frequency waves encountered are modulated by the unsteady underlying current and

therefore the demodulated spectrum can only be estimated locally. This requires use of analog methods.

- (iii) To date, the radar modulation study has excluded the possible scattering effect due to the intermittent short wave breaking. Studies of the drop-out patches in the received optical sensor signal can be used to study short wave breaking characteristics.

APPENDIX A
ALGORITHM FOR ESTIMATING THE WAVE HEIGHT DIRECTIONAL SPECTRUM

Various methods for the estimation of the directional wave height spectrum were proposed for different measured parameters (Longuet-Higgins et al., 1963; Panicker, 1971; Forristall et al., 1978). For the MARSEN Noordwijk tower experiment, the current meter was located at a horizontal distance of $x_0 = 3.66$ m from the location where the surface displacements were measured. Here we proposed an algorithm to estimate the wave height directional spectrum $E(f, \theta)$.

As stated above, we have the surface displacement measurement which is specified as

$$\eta(0,0,t) = \eta(t) = \sum_m \sum_j A_{mj} \cos(-2\pi f_m t + \phi_{mj}). \quad (A-1)$$

Here A_{mj} is the amplitude of the component wave, f_m is the circular frequency which is related to the wavenumber k_m as

$$(2\pi f_m)^2 = g k_m \tanh k_m h,$$

t is the time and ϕ_{mj} is the random phase uniformly distributed on the interval $(0, 2\pi)$. The u-current is specified as

$$u(x_0, 0, t) = u(t) = \sum_m \sum_j A_{mj} \cos \theta_j R_m \cos (k_m x_0 \cos \theta_j - 2\pi f_m t + \phi_{mj}), \quad (A-2)$$

and the v-current component is given by

$$v(x_0, 0, t) = v(t) = \sum_m \sum_j A_{mj} \sin \theta_j R_m \cos(k_m x_0 \cos \theta_j - 2\pi f_m t + \phi_{mj}) , \quad (\text{A-3})$$

where

$$R_m = 2\pi f_m \frac{\cosh k_m z_0}{\sinh k_m h} , \quad (\text{A-4})$$

and

$$A_{mj}^2 = 2E(f_m, \theta_j) \Delta f_m \Delta \theta_j \quad (\text{A-5})$$

In equation (A-4), z_0 is the vertical distance of the sensor above the sea bed, h is the depth of the water ($h = 18$ m).

The cross-correlation function $R(\tau)$ defined as the mean of the product of two functions separated by a lag τ can be derived for three measurements as follows:

$$R_{nu}(\tau) = \sum_m \sum_j \frac{A_{mj}^2}{2} R_m \cos \theta_j \cos(k_m x_0 \cos \theta_j - 2\pi f_m \tau) \quad (\text{A-6})$$

$$R_{nv}(\tau) = \sum_m \sum_j \frac{A_{mj}^2}{2} R_m \sin \theta_j \cos(k_m x_0 \cos \theta_j - 2\pi f_m \tau) \quad (\text{A-7})$$

$$R_{uv}(\tau) = \sum_m \sum_j \frac{A_{mj}^2}{2} R_m^2 \sin \theta_j \cos \theta_j \cos(2\pi f_m \tau) \quad (\text{A-8})$$

$$R_{nn}(\tau) = \sum_m \sum_j \frac{A_{mj}^2}{2} \cos(2\pi f_m \tau) \quad (\text{A-9})$$

$$R_{uu}(\tau) = \sum_m \sum_j \frac{A_{mj}^2}{2} R_m^2 \sin^2 \theta_j \cos(2\pi f_m \tau) \quad (\text{A-10})$$

$$R_{vv}(\tau) = \sum_m \sum_j \frac{A_{mj}^2}{2} R_m^2 \cos^2 \theta_j \cos(2\pi f_m \tau) \quad (\text{A-11})$$

Strictly speaking, equations (A-9) to (A-11) are auto-correlation functions. For the infinitesimal increment of f and θ , we can change

the summation sign to the integral sign for equations (A-6) to (A-11) by using equation (A-5)

$$R_{\eta u}(\tau) = \int_0^{\infty} \int_0^{2\pi} E(f, \theta) R(f) \cos \theta \cos(kx_0 \cos \theta - 2\pi f\tau) d\theta df \quad (\text{A-12})$$

$$R_{\eta v}(\tau) = \int_0^{\infty} \int_0^{2\pi} E(f, \theta) R(f) \sin \theta \sin(kx_0 \cos \theta - 2\pi f\tau) d\theta df \quad (\text{A-13})$$

$$R_{uv}(\tau) = \int_0^{\infty} \int_0^{2\pi} E(f, \theta) R^2(f) \sin \theta \cos \theta \cos(2\pi f\tau) d\theta df \quad (\text{A-14})$$

$$R_{\eta\eta}(\tau) = \int_0^{\infty} \int_0^{2\pi} E(f, \theta) \cos(2\pi f\tau) d\theta df \quad (\text{A-15})$$

$$R_{uu}(\tau) = \int_0^{\infty} \int_0^{2\pi} E(f, \theta) R^2(f) \cos^2 \theta \cos(2\pi f\tau) d\theta df \quad (\text{A-16})$$

$$R_{vv}(\tau) = \int_0^{\infty} \int_0^{2\pi} E(f, \theta) R^2(f) \sin^2 \theta \cos(2\pi f\tau) d\theta df \quad (\text{A-17})$$

The Weiner-Khinchine relation (Bendat and Piersol, 1971) implies

$$E_{\eta u}(f) = 2 \int_{-\infty}^{\infty} R_{\eta u}(\tau) e^{-i2\pi f\tau} d\tau \quad (\text{A-18})$$

$$\equiv C_{\eta u}(f) - i Q_{\eta u}(f), \quad (\text{A-19})$$

where $C_{\eta u}$ is called the co-spectrum and $Q_{\eta u}$ is called the quad-spectrum.

The reverse relation can be written as

$$R_{\eta u}(\tau) = \int_0^{\infty} [C_{\eta u}(f) \cos(2\pi f\tau) + Q_{\eta u}(f) \sin(2\pi f\tau)] df. \quad (\text{A-20})$$

Comparing equations (A-20) and (A-12), we have

$$C_{nu}(f) = R(f) \int_0^{2\pi} E(f, \theta) \cos \theta \cos(kx_0 \cos \theta) d\theta \quad (A-21)$$

and

$$Q_{nu}(f) = R(f) \int_0^{2\pi} E(f, \theta) \cos \theta \sin(kx_0 \cos \theta) d\theta . \quad (A-22)$$

Similarly, equations (A-13) and (A-14) can be reduced to

$$C_{nv}(f) = R(f) \int_0^{2\pi} E(f, \theta) \sin \theta \cos(kx_0 \sin \theta) d\theta \quad (A-23)$$

$$Q_{nv}(f) = R(f) \int_0^{2\pi} E(f, \theta) \sin \theta \sin(kx_0 \sin \theta) d\theta \quad (A-24)$$

$$C_{uv}(f) = R^2(f) \int_0^{2\pi} E(f, \theta) \sin \theta \cos \theta d\theta \quad (A-25)$$

The auto-correlation function can be derived from the auto-spectrum, for example

$$R_{nn}(\tau) = \int_0^{\infty} E_{nn}(f) e^{i2\pi f\tau} df .$$

compared with (A-15), we have

$$E_{nn}(f) = \int_0^{2\pi} E(f, \theta) d\theta \quad (A-26)$$

Similarly, we can derive

$$E_{uu}(f) = R^2(f) \int_0^{2\pi} E(f, \theta) \cos^2 \theta d\theta \quad (A-27)$$

and

$$E_{vv}(f) = R^2(f) \int_0^{2\pi} E(f, \theta) \sin^2 \theta d\theta \quad (A-28)$$

Now, we let

$$E(f, \theta) = E(f) D(\theta) \quad (A-29)$$

where $D(\theta)$ is the angular spreading function and is a function of frequency in general. Equations (A-21) to (A-28) can be written as

$$C_{nu}(f) = E(f) R(f) \int_0^{2\pi} D(\theta) \cos \theta \cos(kx_0 \cos \theta) d\theta \quad (A-30)$$

$$Q_{nu}(f) = E(f) R(f) \int_0^{2\pi} D(\theta) \cos \theta \sin(kx_0 \sin \theta) d\theta \quad (A-31)$$

$$C_{nv}(f) = 2E(f) R(f) \int_0^{2\pi} D(\theta) \sin \theta \cos(kx_0 \sin \theta) d\theta \quad (A-32)$$

$$Q_{nv}(f) = 2E(f) R(f) \int_0^{2\pi} D(\theta) \sin \theta \sin(kx_0 \sin \theta) d\theta \quad (A-33)$$

$$C_{uv}(f) = E(f) R^2(f) \int_0^{2\pi} D(\theta) \cos \theta \sin \theta d\theta \quad (A-34)$$

$$E_{nn}(f) = E(f) \int_0^{2\pi} D(\theta) d\theta \quad (A-35)$$

$$E_{uu}(f) = E(f) R^2(f) \int_0^{2\pi} D(\theta) \cos^2 \theta d\theta \quad (A-36)$$

$$E_{vv}(f) = E(f) R^2(f) \int_0^{2\pi} D(\theta) \sin^2 \theta d\theta \quad (A-37)$$

Now, we expand $D(\theta)$ in the Fourier series

$$D(\theta) = \frac{1}{2\pi} + \frac{1}{\pi} \sum_{n=1}^{\infty} (a_n \cos n\theta + b_n \sin n\theta) \quad (A-38)$$

$$\approx \frac{1}{2\pi} + \frac{1}{\pi} \sum_{n=1}^2 (a_n \cos n\theta + b_n \sin n\theta)$$

as the first approximation. (A-35) implies

$$E(f) = E_{nn}(f) \quad (A-39)$$

Equations (A-36) and (A-37) imply

$$\frac{E_{uu} - E_{vv}}{ER^2} = \int_0^{2\pi} D(\theta) \cos 2\theta \, d\theta = a_2 \quad (\text{A-40})$$

Equation (A-34) gives

$$\frac{C_{uv}}{ER^2} = \frac{1}{2} \int_0^{2\pi} D(\theta) \sin 2\theta \, d\theta = \frac{b_2}{2} \quad (\text{A-41})$$

Equations (A-30) and (A-31) imply

$$\frac{C_{nu} + i Q_{nu}}{ER} = \int_0^{2\pi} D(\theta) \cos \theta \, e^{ikx_0 \cos \theta} \, d\theta \quad (\text{A-42})$$

From the identities (see Abramowitz and Stegun, 1965)

$$J_n(x_0) = \frac{i^{-n}}{\pi} \int_0^{2\pi} e^{ix_0 \cos \theta} \cos(n\theta) \, d\theta \quad (\text{A-43})$$

and

$$\int_0^{2\pi} e^{ikx_0 \cos \theta} \sin(n\theta) \, d\theta = 0 \quad , \quad (\text{A-44})$$

equation (A-41) gives

$$\frac{C_{nu}}{ER} = a_1 [J_0(kx_0) - J_2(kx_0)] \quad (\text{A-45})$$

and

$$\frac{Q_{nu}}{ER} = J_1(kx_0) + a_2 [J_1(kx_0) - J_3(kx_0)] \quad (\text{A-46})$$

Similarly, equations (A-32) and (A-33) give

$$\frac{C_{nv}}{ER} = b_1 [J_0(kx_0) + J_2(kx_0)] \quad (\text{A-47})$$

$$\frac{Q_{nV}}{ER} = b_2[J_1(kx_0) + J_3(kx_0)] . \quad (\text{A-48})$$

In summary, we have

$$E(f) = E_{\eta\eta}(f) \quad (\text{A-39})$$

$$a_1 = C_{nU}/[ER(J_0 - J_2)] \quad (\text{A-45})$$

$$\begin{aligned} a_2 &= (E_{UU} - E_{VV})/ER^2 \quad (\text{A-40, 46}) \\ &= \left(\frac{Q_{nU}}{ER} - J_1\right)/(J_1 - J_3) \end{aligned}$$

$$b_1 = C_{nV}/[ER(J_0 + J_2)] , \quad (\text{A-47})$$

and

$$\begin{aligned} b_2 &= 2C_{UV}/ER^2 \quad (\text{A-41, 48}) \\ &= Q_{nV}/[ER(J_1 + J_3)] . \end{aligned}$$

Because we select only two terms in the expansion of $D(\theta)$, we need weighting coefficients W_1 and W_2 such that

$$E(f, \theta) = \frac{E(f)}{\pi} \left[\frac{1}{2} + \sum_{n=1}^2 W_n (a_n \cos n\theta + b_n \sin n\theta) \right] \quad (\text{A-49})$$

where

$$W_1 = 2/3 , \quad W_2 = 1/6 \quad (\text{Longuet-Higgins, et al, 1963}). \quad (\text{A-50})$$

The dominant wave direction $\bar{\theta}$ for a particular Fourier component is given by

$$\bar{\theta}(f) = \tan^{-1} \frac{b_1(f)}{a_1(f)} . \quad (\text{A-51})$$

APPENDIX B
DEMODULATION PROCEDURE

Preparation of the Input Data

There are four input data records to be used for the demodulation of the slope signals. The slope signal $s(t)$ measured by the laser-optical sensor is the signal to be demodulated for a given wavelength band. The wave directional distribution, $\bar{\theta}(f)$, derived from the directional spectrum (see Appendix A) covers the frequency range from 0.05 to 0.46 Hz. The tidal current is calculated from the D.C. component of the current record.

The sea surface displacement, $\eta(t)$, is calculated from both the wave follower displacement signal and the error signal. $\eta(t)$ and $\bar{\theta}(f)$ are used to calculate the surface orbital velocity as described in the following.

Calculation of Long Wave Doppler Effects on Short Waves

We first transform the sea surface displacement $\eta(t)$ to the frequency domain and then calculate the velocity for each Fourier component as follows

$$\tilde{u}(f) = a(f) 2\pi f \coth kh, \quad (B-1)$$

where $a(f)$ is the Fourier coefficient. We then calculate the contribution of $\tilde{u}(f)$ in the down-wind direction

$$\tilde{v}(f) = \tilde{u}(f) \cos(\bar{\theta} - \theta_a). \quad (B-2)$$

Finally, we take the inverse Fourier transform to get the time function of the surface orbital velocity component in the down-wind direction.

Band Consideration of Short Waves

For a selected wavelength band (λ_-, λ_+) , the central wavelength is defined by

$$\lambda_s = (\lambda_+ + \lambda_-)/2 \quad (B-3)$$

which is used as the wavelength parameter in the capillary-gravity phase speed expression

$$C_s^2 = g/k_s + \Gamma k_s / \rho, \quad (B-4)$$

where

$$k_s = 2\pi/\lambda_s. \quad (B-5)$$

Because of the wind-drift, the short wave phase speed is enhanced by the surface drift which is specified as

$$V_s = C_s + 0.03 U_a. \quad (B-6)$$

where U_a is the wind speed.

The medium travel speed along the direction of the short wave is given by

$$V_m = V_l + V_t \quad (B-7)$$

where V_l and V_t represent the horizontal surface orbital velocity of long waves and the tidal current in the direction of short wave travel respectively.

The equivalent distance corresponding to the slope signal of duration T is

$$\lambda_T = \int_T |V_s + V_m| dt \quad . \quad (B-8)$$

Demodulation for the Slope Signal s(t) of duration T

Since the measured slope signal s(t) is sampled at a constant time interval, the equivalent spatial distribution of the slope signal is not even in nature. To remedy this, we use an interpolation scheme to get the equally-distributed slope signal in the spatial domain. We then apply FFT on the interpolated slope data to get the distribution in the wavenumber domain.

After band-passing the selected wavelength band of the slope signal in the wavenumber domain, we transform the signal back to the spatial domain. The signal is then transformed back to the time domain where the sampling rate is reduced to 25 sps by taking the mean square value of the neighboring signal values. The demodulated mean-squared slope signal is thus obtained.

REFERENCES

- Abramowitz, M., and Stegun, I.A. (1965), Handbook of Mathematical Functions, Dover, New York.
- Alpers, W., and Hasselmann, K. (1978), The two-frequency microwave technique for measuring ocean-wave spectra from an airplane or satellite, Boundary-Layer Meteorol., 14, 215-230.
- Banner, M.L., and Melville, W.K. (1976), On the separation of air flow over water waves, J. Fluid Mech., 77, 825-842.
- Banner, M.L., and Phillips, O.M. (1974), On the incipient breaking of small scale waves, J. Fluid Mech., 65, 647-656.
- Barnett, T.P., and Wilkerson, J.C. (1967), On the generation of ocean wind waves as inferred from airborne radar measurements of fetch-limited spectra, J. Mar. Res., 25, 292-321.
- Bendat, J.S., and Piersol, A.G. (1971), Random data: Analysis and measurement procedures, John Wiley, N.Y.
- Bowden, K.F., and White, R.A. (1966), Measurements of the orbital velocities of sea waves and their use in determining the directional spectrum, Geophys. J. Roy. Astron. Soc., 12, 33-54.
- Cox, C.S. (1958), Measurements of slopes of high frequency wind waves, J. Mar. Res., 16, 199-225.
- Cox, C.S., and Munk, W.H. (1954), Statistics of the sea surface derived from sun glitter, J. Mar. Res., 13, 198-227.
- Dorman, C.E., and Mollo-Christensen, E. (1973), Observation of the structure of moving gust patterns over a water surface ('cat paws'), J. Phys. Oceanogr., 3, 120-132.
- Evans, D.D., and Shemdin, O.H. (1980), An investigation of the modulation of capillary and short gravity waves in the open ocean, J. Geophys. Res., 85, 5019-5024.
- Forristall, G.Z., Ward, E.G., Cardone, V.J., and Borgmann, L.E. (1973), The directional spectra and kinematics of surface gravity waves in tropical storm Delia, J. Phys. Oceanogr., 8, 888-909.
- Garrett, C., and Smith, J. (1976), On the interaction between long and short surface waves, J. Phys. Oceanogr., 6, 925-930.

- Gent, P.R., and Taylor, P.A. (1976), A numerical model of the air flow above water waves, J. Fluid Mech., 77, 105-128.
- Hasselmann, K. (1971), On the mass and momentum transfer between short gravity waves and larger-scale motions, J. Fluid Mech., 50, 189-205.
- Hasselmann, K., Barnett, T.P., Bouws, E., Carlson, H., Cartwright, D.E., Enke, K., Ewing, J.A., Gienapp, H., Hasselmann, D.E., Kruseman, P., Meerburg, A., Muller, P., Olbers, D.J., Richter, K., Sell, W., and Walden, H. (1973), Measurements of wind-wave growth and swell decay during the joint North Sea wave project (JONSWAP), Dtsch. Hydrogr. Z., Suppl. A., 8(12).
- Huang, N.E. (1979), On surface drift currents in the ocean, J. Fluid Mech., 91, 191-208.
- Keller, W.C., and Wright, J.W. (1975), Microwave scattering and the straining of wind-generated waves, Radio Sci., 10, 139-147.
- Krogh, F.T. (1970), FRT1-one dimensional real Fourier transform, Tech. Brief, CP-2310, Jet Prop. Lab., Pasadena, California.
- Liu, P.C. (1971), Normalized and equilibrium spectra of wind waves in Lake Michigan, J. Phys. Oceanogr., 1, 249-257.
- Lleonart, G.T., and Blackman, D.R. (1980), The spectral characteristics of wind-generated capillary waves, J. Fluid Mech., 97, 455-479.
- Long, S.R., and Huang, N.E. (1976), On the variation and growth of wave-slope spectra in the capillary-gravity range with increasing wind, J. Fluid Mech., 77, 209-228.
- Longuet-Higgins, M.S. (1969), A nonlinear mechanism for the generation of sea waves, Proc. Roy. Soc. London, A, 311, 371-389.
- Longuet-Higgins, M.S., Cartwright, D.E., and Smith, N.D. (1963), Observations of the directional spectrum of sea waves using the motions of a floating buoy, Ocean Wave Spectra, Prentice-Hall, N.J.
- Longuet-Higgins, M.S., and Stewart, R.W. (1960), Changes in the form of short gravity waves on long waves and tidal currents, J. Fluid Mech., 8, 565-583.
- Longuet-Higgins, M.S., and Stewart, R.W. (1964), Radiation stresses in water waves: A physical discussion with applications, Deep Sea Res., 11, 529-562.
- McLeish, W., Ross, D., Shuchman, R.A., Teleki, P.G. Hsiao, S.V., Shemdin, O.H., and Brown, W.E., Jr. (1980), Synthetic aperture radar imaging of ocean waves: Comparison with wave measurements, J. Geophys. Res., 85, 5003-5011.
- Miles, J.W. (1957), On the generation of surface waves by shear flows, J. Fluid Mech., 3, 185-204.

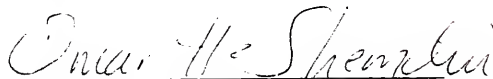
- Miles, J.W. (1960), On the generation of surface waves by turbulent shear flows, J. Fluid Mech., 7, 469-478.
- Mitsuyasu, H. (1966), Interactions between water waves and wind (I), Rep. Res. Inst. Appl. Mech., Kyushu Univ., 14, 67-88.
- Mitsuyasu, H. (1977), Measurement of high-frequency spectrum of ocean surface waves, J. Phys. Oceanogr., 7, 882-891.
- Mitsuyasu, H., and Honda, T. (1974), The high frequency spectrum of wind-generated waves, J. Oceanogr. Soc. Japan, 30, 185-198.
- Newland, D.E. (1975), An introduction to random vibrations and spectral analysis, Longman, London.
- Olson, J.R. (1972), Two-component electromagnetic flowmeter, Marine Tech. Soc. J., 6, 19-24.
- Palm, C.S. (1975), An instrument to measure the two dimensional wave slope spectrum of ocean capillary waves, Ph.D. Dissertation, University of Florida, Gainesville, Florida.
- Panicker, N.N. (1971), Determination of directional spectra of ocean waves from gage arrays, Technical Report, HEL 1-18, University of California, Berkeley.
- Pawka, S.S., Hsiao, S.V., Shemdin, O.H., and Inman, D.L. (1980), Comparison between wave directional spectra from SAR and pressure sensor arrays, J. Geophys. Res., 85, 4987-4995.
- Phillips, O.M. (1957), On the generation of waves by turbulent wind, J. Fluid Mech., 2, 417-445.
- Phillips, O.M. (1958), The equilibrium range in the spectrum of wind-generated waves, J. Fluid Mech., 4, 426-434.
- Phillips, O.M. (1963), On the attenuation of long gravity waves by short breaking waves, J. Fluid Mech., 16, 321-332.
- Phillips, O.M. (1977), The dynamics of the upper ocean, Cambridge University Press, Cambridge.
- Pierson, W.J. (1976), The theory and applications of ocean wave measuring systems at and below the sea surface, on the land, from aircraft, NASA Contractor Rep. CR-2646, 400 pp.
- Plant, W.J. (1980), Measurement of ocean wave-radar modulation transfer function, personal communications.
- Reece, A.M. (1978), Modulation of short wave by long waves, Boundary-Layer Meteorol., 14, 203-214.

- Schooley, A.H. (1958), Profiles of wind-created water waves in the capillary-gravity transition region, J. Mar. Res., 16, 100-108.
- Shemdin, O.H. (1972), Wind generated current and phase speed of wind waves, J. Phys. Oceanogr., 2, 411-419.
- Shemdin, O.H. (1981), Measurement of wind and surface wave slopes with a wave follower, Final Report, Jet Prop. Lab., Pasadena, California.
- Snyder, R.L., and Cox, C.S. (1966), A field study of the wind generation of ocean waves, J. Mar. Res., 24, 141-178.
- Tober, G., Anderson, R.C., and Shemdin, O.H. (1973), Laser instrument for detecting water ripple slopes, Appl. Opt., 12, 788-794.
- Townsend, A.A. (1972), Flow in a deep turbulent boundary layer over a surface distorted by water waves, J. Fluid Mech., 55, 719-735.
- Ursell, F. (1956), Wave generation by wind, Surveys in Mechanics (ed. G.K. Batchelor), pp. 216-249, Cambridge University Press, Cambridge.
- Valenzuela, G.R. (1978), Theories for the interaction of electromagnetic and oceanic waves--A review, Boundary-Layer Meteorol., 13, 61-85.
- Welch, P.D. (1967), The use of FFT for the estimation of power spectra: A method based on time averaging over short, modified periodograms, IEEE Trans. Audio Electroacoust. AU-15, 70-73.
- Winant, C.D., and Olson, J.R. (1976), The vertical structure of coastal currents, Deep-Sea Res., 23, 925-936.
- Wright, J.W. (1976), The Wind Drift and Wave Breaking, J. Phys. Oceanogr., 7, 402-405.
- Wright, J.W., Plant, W.J., Keller, W.C., and Jones, W.L. (1980), Ocean wave-radar modulation transfer functions from the West Coast Experiment, J. Geophys. Res., 85, 4957-4966.
- Wu, J. (1971), Slope and curvature distributions of wind-disturbed water surface, J. Opt. Soc. Am., 61, 852-858.

BIOGRAPHICAL SKETCH

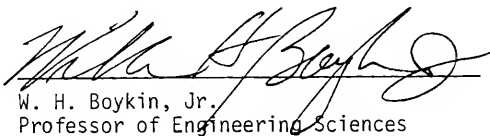
Shih-Tsan Tang was born in Taipei, Taiwan, in September 1949. He received his Bachelor of Science degree from National Central University, Chungli, Taiwan, in 1973 and his Master of Science degree in physical oceanography from National Taiwan University, Taipei, Taiwan, in 1975. He was at Purdue University, West Lafayette, Indiana, before starting his Ph.D. work at the University of Florida in September 1977.

I certify that I have read this study and that in my opinion it conforms to acceptable standards of scholarly presentation and is fully adequate, in scope and quality, as a dissertation for the degree of Doctor of Philosophy.



O. H. Shemdin, Chairman
Professor of Engineering Sciences and
Coastal and Oceanographic Engineering

I certify that I have read this study and that in my opinion it conforms to acceptable standards of scholarly presentation and is fully adequate, in scope and quality, as a dissertation for the degree of Doctor of Philosophy.



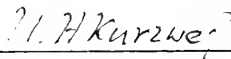
W. H. Boykin, Jr.
Professor of Engineering Sciences

I certify that I have read this study and that in my opinion it conforms to acceptable standards of scholarly presentation and is fully adequate, in scope and quality, as a dissertation for the degree of Doctor of Philosophy.



C. C. Hsu
Professor of Engineering Sciences

I certify that I have read this study and that in my opinion it conforms to acceptable standards of scholarly presentation and is fully adequate, in scope and quality, as a dissertation for the degree of Doctor of Philosophy.



U. H. Kurzweg
Professor of Engineering Sciences

I certify that I have read this study and that in my opinion it conforms to acceptable standards of scholarly presentation and is fully adequate, in scope and quality, as a dissertation for the degree of Doctor of Philosophy.

Michael X. Ochi

M. K. Ochi
Professor of Coastal and Oceanographic
Engineering

I certify that I have read this study and that in my opinion it conforms to acceptable standards of scholarly presentation and is fully adequate, in scope and quality, as a dissertation for the degree of Doctor of Philosophy.

Arun Kumar Varma

A. K. Varma
Professor of Mathematics

This dissertation was submitted to the Graduate Faculty of the College of Engineering and to the Graduate Council, and was accepted as partial fulfillment of the requirements for the degree of Doctor of Philosophy.

December 1981

Herbert A. Bevis

Dean, College of Engineering

Dean for Graduate Studies and Research

UNIVERSITY OF FLORIDA



3 1262 08553 3668